Emergence of Inertial Gyres in a Two-Layer Quasigeostrophic Ocean Model

TAMAY M. ÖZGÖKMEN AND ERIC P. CHASSIGNET

RSMAS/MPO, University of Miami, Miami, Florida

ABSTRACT

The emergence of Fofonoff-like flows over a wide range of dissipative parameter regimes is explored in a wind-driven two-layer quasigeostrophic model. Two regimes are found in which Fofonoff-like circulations emerge as a direct consequence of the baroclinic nature of the system, since the wind forcing used in these experiments has been shown to inhibit the formation of Fofonoff flows in the barotropic case. The first regime is one in which the magnitudes of the frictional coefficients (viscosity and bottom dissipation) are extremely small. The experiments clearly illustrate the transition of the numerical solution from a conventional wind-driven circulation to an inertial Fofonoff-like regime. The latter circulation first appears in the lower layer and then spreads throughout the water column via barotropization. The second regime, surprisingly, is obtained with very high bottom friction. This result indicates that entropy can be maximized independently in each layer, depending on the distribution of forcing and dissipation. This sheds a new perspective on the common assumption that forcing and dissipation are disruptive effects that prevent the system from displaying a Fofonoff state.

1. Introduction

The investigation of nonlinear processes is of primary importance in developing our understanding of the large-scale general ocean circulation. It is generally accepted that the nonlinear inertial terms are important in regions such as western boundary currents and midlatitude jets (e.g., Harrison and Holland 1981), and that these terms are responsible for the formation of recirculating gyres, which enhance the transport of important current systems such as the Gulf Stream and the Kuroshio many times over the corresponding linear Sverdrup wind-driven transport. The effect of the nonlinear inertial terms is quite different from that of other processes in the ocean. Unlike wind forcing, heat exchange with the atmosphere, or frictional effects, inertial processes do not have a net contribution to the energy budget. Their major role appears to be in the reorganization of the flow generated by other mechanisms. It is therefore important to explore and understand the flow characteristics to which the inertial terms tend to drive the system.

Inertial modes were first sought by Fofonoff (1954), who considered steady solutions of a frictionless, homogeneous fluid in a rectangular ocean basin of constant depth on a beta plane. His solution is characterized by a linear relationship between potential vorticity and streamfunction and possesses intense inertial boundary layers along the western, eastern, and zonal boundaries of the domain, accompanied by a uniform zonal flow elsewhere. When the total vorticity of the system is zero, the solution consists of two antisymmetric gyres, an anticyclonic gyre in the northern basin and a cyclonic gyre in the southern basin (Fig. 1a). When the total vorticity is positive (negative), the cyclonic (anticyclonic) gyre then prevails. The significance of Fofonoff's (1954) solution was not clear until Veronis (1966) pointed to a visual resemblance between his own numerical simulations of a barotropic wind-driven ocean consisting of a single gyre and Fofonoff's solution when nonlinear effects dominated.

Theoretically, Salmon et al. (1976, hereafter SHH), using equilibrium statistical mechanics, demonstrated that Fofonoff's solution corresponds to the mean flow of a stable equilibrium state in which the entropy of the system is maximized. Independently, Bretherton and Haidvogel (1976) showed that Fofonoff's solution also resulted from the minimum enstrophy states of the system. That the maximum entropy equilibrium actually coincides with the minimum enstrophy state in the limit of infinite resolution was shown by Carnevale and Fredericksen (1987).

The derivations by SHH were based on the assumption of unforced and undamped quasigeostrophic flows. In an attempt to understand the impact of both forcing and dissipation on the emergence of Fofonoff gyres, Griffa and Salmon (1989, hereafter GS) carried out numerical simulations using the barotropic quasigeostrophic equation in a beta-plane, flat-bottomed basin.

Corresponding author address: Dr. Tamay M. Özgökmen, RSMAS/MPO,University of Miami, 4600 Rickenbacker Causeway, Miami, FL 33149-1098.
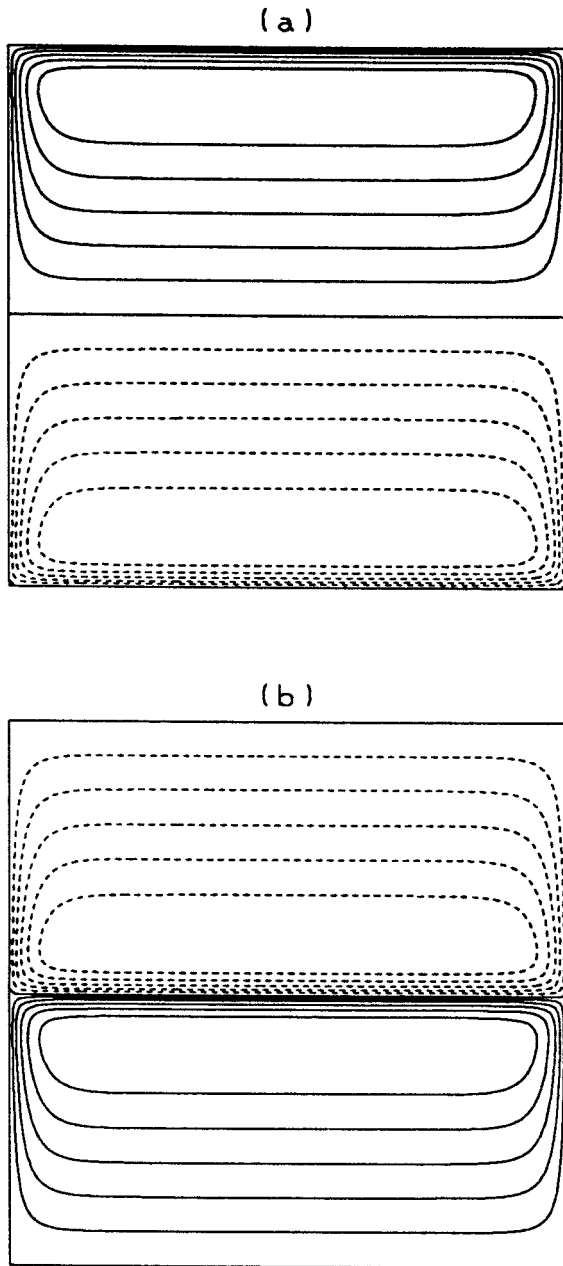E-mail: tamay@obelix.rsmas.miami.edu

(a)

(b)

FIG. 1. (a) Fofonoff solution of a homogeneous fluid in a rectangular basin of constant depth on a beta plane. (b) Upper-layer flow based on the steady solutions of stratified quasigeostrophic dynamics with weak forcing and dissipation as in Marshall and Nurser (1986). Solid lines indicate anticyclonic circulation and dashed lines cyclonic circulation.

They found that the nonlinear terms still tended to drive the flow toward the Fofonoff gyres, but that this result depended strongly on the *geometry* of the wind stress. If the prescribed wind stress exerted a torque that acted to balance the bottom-drag torque around every closed streamline of the Fofonoff flow, then the solutions were energetic and Fofonoff-like. If, on the other hand, the wind opposed the Fofonoff flow, the solutions then ex-

hibited small mean flows with much less energy, and the Fofonoff gyres did not emerge.

The wind stress distribution over the North Atlantic Ocean acts to drive a cyclonic (subpolar) gyre in the north and an anticyclonic (subtropical) gyre in the south. According to the results of GS, this kind of wind forcing is incompatible with the Fofonoff flows, and one may then conclude that inertial states are not allowed in this configuration. However, conclusions by GS were based on the barotropic quasigeostrophic equation, where the wind and bottom torques both act throughout the water column. In the ocean, these two forces are actually separated by the effect of stratification: The wind stress transfers momentum to the upper ocean, whereas the bottom torque acts mostly on the deeper layers. It is therefore of interest to investigate the possibility for the emergence of Fofonoff gyres in a forced–dissipative system when the dividing effect of stratification is included.

When baroclinicity was introduced by SHH with two-layer quasigeostrophic flows, they demonstrated that, for the unforced inviscid case, the equilibrium flow was nearly barotropic at scales of motion larger than the radius of deformation, while at smaller scales the streamfunctions in the two layers were statistically uncorrelated. Marshall and Nurser (1986) studied the steady solutions of a stratified quasigeostrophic flow with weak forcing and dissipation. Their analytical solutions are characterized by a linear relationship between streamfunction and potential vorticity in the upper layer, as for the Fofonoff solution. However, the sign of the proportionality constant is negative, rather than positive as in the conventional Fofonoff solution. The resulting circulation is opposite to that of the conventional Fofonoff flow (Fig. 1a), with two gyres divided by a strong jet (Fig. 1b). In the lower layer, the potential vorticity is homogenized as in the theory of Rhines and Young (1982).

The purpose of this paper is to explore the emergence of inertial gyres in a forced–dissipative baroclinic system represented by a two-layer quasigeostrophic model. In the two-layer system, the lower layer, while not directly exposed to wind forcing, still receives energy via barotropic and baroclinic instabilities taking place in the system. By analogy to the barotropic case, it is hypothesized that the lower-layer flow can take the shape of Fofonoff gyres in the limit of small dissipation. By conducting numerical simulations, we demonstrate that inertial gyres that are Fofonoff-like (circulation in the same direction as the conventional barotropic Fofonoff flow) can actually emerge in a two-layer system despite the fact that the wind torque acts to oppose this flow.

The paper is organized as follows: The numerical model is introduced in section 2. In section 3, the configuration of the model is described and the main characteristics of the numerical experiments are presented in section 4. The results are discussed in section 5 and summarized in the concluding section.

TABLE 1. List of the numerical experiments. In all experiments, the domain is centered at 40°N and shares the same upper-layer depth scale $h_0 = 1000$ m, total fluid depth scale $H = 5000$ m, and reduced gravity $g' = 0.02$ m s^{-2}. The parameters for experiments VI and VII are the same as those for experiments III and V except for reversed wind forcing.

Parameter	Experiment						
	I	II	III	IV	V	VI	VII
l (km)	2000	2000	2000	2000	3500	2000	3500
Resolution	151^2	301^2	301^2	301^2	301^2	301^2	301^2
ν (m^2 s^{-1})	50.0	1.5	0.0	0.0	0.0	0.0	0.0
r (s^{-1})	5×10^{-8}	5×10^{-8}	5×10^{-8}	1×10^{-9}	5×10^{-4}	5×10^{-8}	5×10^{-4}
Ro $= U_{rms}/\beta l^2$	2×10^{-3}	2×10^{-3}	2×10^{-3}	3×10^{-3}	4.5×10^{-3}	6.6×10^{-3}	7×10^{-3}
δ_L (km)	14.2	4.4	0.0	0.0	0.0	0.0	0.0
δ_B (km)	2.9	2.9	2.9	0.06	2.9×10^4	2.9	2.9×10^4
δ_I (km)	31.7	31.7	31.7	41.6	95.4	70.2	128.0

2. The numerical model

The quasigeostrophic model used in this study is similar to the one developed by Holland (1978). The governing equations can be written in nondimensional form as

$$q_{1t} + J(\psi_1, q_1) = \frac{w_E}{\delta} + A\nabla^4\psi_1 \qquad (1)$$

$$q_{2t} + J(\psi_2, q_2) = A\nabla^4\psi_2 - \sigma\nabla^2\psi_2, \qquad (2)$$

where q_1 and q_2 are the upper- and lower-layer potential vorticities given by

$$q_1 = y + \frac{F}{\delta}(\psi_2 - \psi_1) + R\nabla^2\psi_1 \qquad (3)$$

$$q_2 = y + \frac{F}{1-\delta}(\psi_1 - \psi_2) + R\nabla^2\psi_2, \qquad (4)$$

and ψ_1 and ψ_2 are the upper- and lower-layer streamfunctions defined as

$$\psi_1 = \frac{\beta H}{f_0^2 Wl}\left(g'\eta + \frac{p}{\rho_0}\right) \quad \text{and} \quad \psi_2 = \frac{\beta H}{f_0^2 Wl}\frac{p}{\rho_0}. \quad (5)$$

Here $w_E(x, y)$ is the Ekman pumping distribution, W its amplitude, l the domain length scale, $p(x, y, t)$ the lower-layer pressure, h_0 the upper-layer depth scale, $\eta(x, y, t)$ the interface displacement (positive downward), H the total domain depth scale, g' the reduced gravity, ρ_0 the reference (upper layer) density, f_0 the Coriolis frequency at a reference latitude, β the meridional gradient of the Coriolis frequency, ν the lateral viscosity coefficient, and r the bottom friction coefficient. The nondimensional parameters are defined as the layer ratio $\delta = h_0/H$, the basin Rossby number (based on forcing) $R = f_0 W/\beta^2 Hl = V/\beta l^2$, the Froude number $F = f_0^3 W/g'\beta^2 H^2 = V/\beta\delta R_d^2$, the lateral friction parameter $A = \nu/\beta l^3$, the bottom friction parameter $\sigma = r/\beta l$, where $V = f_0 W/\beta H$ is the barotropic Sverdrup velocity scale, and $R_d = (g'h_0)^{1/2}/f_0$ the internal radius of deformation.

The prognostic equations (1) and (2) are advanced in time using a predictor-corrector type leapfrog method (Gazdag 1976). Variable time stepping is employed to obtain high efficiency during the spinup phase and to reduce the influence of numerical errors. The Jacobian operator $J(a, b) = a_x b_y - a_y b_x$ is computed using the formulation proposed by Arakawa (1966) that conserves kinetic energy, enstrophy, and the property $J(a, b) = -J(b, a)$. The diagnostic equations (3) and (4) are inverted using fast Fourier transform techniques.

3. Configuration of the numerical model

The behavior of the two-layer quasigeostrophic model described in the previous section, when configured with various dissipative mechanisms, is investigated in detail in a series of numerical experiments (summarized in Table 1). All experiments are configured in a flat-bottom square basin of length equal to 2000 km (except for expts. V and VII, which have a basin length of 3500 km). This domain size is less than that of a typical ocean basin, but the net result is an increased effective Rossby number, which then permits a better resolution of the inertial boundary layers as well as larger inertial gyres with respect to the basin size (cf. GS; Cummins 1992). The domain is centered on 40°N. The upper-layer and total depth scales are $h_0 = 1000$ m and $H = 5000$ m, respectively. The chosen reduced gravity $g' = 0.02$ m s^{-2} yields a radius of deformation of approximately 43 km, typical of midlatitude ocean circulation.

In most experiments, the ocean is forced by an Ekman pumping distribution of the form

$$w_E(y) = W \sin\left(2\pi\frac{y}{l}\right) \quad \text{with} \quad -\frac{l}{2} \leq y \leq \frac{l}{2}. \quad (6)$$

This forcing generates an anticyclonic (subtropical) gyre in the southern half of the domain and a cyclonic (subpolar) gyre in the northern half. Therefore, it is "unfavorable" for the emergence of Fofonoff gyres. The chosen Ekman pumping amplitude ($W = 2.85 \times 10^{-6}$ m s^{-1} for $l = 2000$ km and $W = 1.63 \times 10^{-6}$ m s^{-1} for $l = 3500$ km) generates a western boundary transport of approximately 30 Sv (Sv $\equiv 10^6$ m^3 s^{-1}) in the conventional Sverdrup (i.e., noninertial) regime. Therefore, it is roughly consistent with the annual mean forcing in the North Atlantic Ocean.

No slip (zero tangential velocity) or free slip (zero

vorticity) are the usual boundary conditions adopted by numerical modelers. The effect of different boundary conditions on the development of inertial circulations was explored by Cummins (1992), who showed that free-slip boundary conditions facilitated the development of Fofonoff gyres when compared to no-slip conditions. No-slip boundary conditions actually inhibited the formation of Fofonoff gyres at moderately high Reynolds number. The influence of different subgrid-scale parameterizations such as Laplacian and biharmonic operators was investigated by Wang and Vallis (1994), who concluded that the boundary condition was generally more important than the order of the viscosity in determining the emergence of Fofonoff gyres. In this study, we opted to employ free-slip boundary conditions with the conventional Laplacian dissipation of momentum. In the experiments performed with zero viscosity, the viscous dissipation operator had no influence on the outcome. The boundary condition for the vorticity can still influence the solution via the nonlinear advective term.

4. Description of the experiments

The focus of this paper is the exploration of the sensitivity of inertial gyres to the frictional parameters: eddy viscosity ν and bottom friction coefficient r. The parameters conventionally chosen in most idealized numerical ocean simulations are, in general, quite large [$\nu \approx O(100 \text{ m}^2 \text{ s}^{-1})$ and $r \approx O(10^{-7} \text{ s}^{-1})$], and Fofonoff-like gyres are not favored. For these parameter choices, frictional boundary layers are formed, and the system is far away from the free state of maximum entropy.

A decrease in eddy viscosity will induce the upper layer to become more unstable, and more energy will then be transferred to the lower layer. Similarly, the energy level in the lower layer will increase as the bottom friction coefficient is reduced. Hence, as frictional parameters are gradually reduced, we expect that more energy will become available, nonlinear interactions will dominate, the entropy of the system will increase, and the system may tend toward a Fofonoff-like mean flow, depending on the influence of the wind forcing (GS).

This trend is first investigated in experiments I–IV by gradually reducing ν and r. A final Rossby number defined as Ro = $U_{\text{rms}}/\beta l^2$, where U_{rms} is the larger rms velocity of the two layers, is typically 10^{-3}–10^{-2}, so that the QG approximation remains valid. The model runs are integrated for 10–20 years until the energetics approach a statistical steady state. The final statistics are then performed over the 5 subsequent years. Integrations of this length are satisfactory for all experiments, except for experiment IV, in which the frictional-damping timescale of about 30 yr causes the model to require a much longer time to reach equilibrium. Since that length of time would create a large computational load, this integration (expt IV) was not carried out to a perfect statistical steady state. Experiment V explores the development of inertial gyres when the system is inviscid, but damped by a very large bottom friction coefficient. Finally, the nature of the gyres developing in experiments with ''unfavorable'' wind forcing is explored by reversing the direction of the wind forcing (in expts VI and VII) such that it favors Fofonoff gyres. Energy budgets are performed for most experiments in order to diagnose the various energy pathways.

It is useful to define the thickness of the boundary layers generated by frictional and inertial processes. The corresponding Munk scale for the viscous boundary layer thickness δ_L is given by

$$\delta_L = \left(\frac{\nu}{\beta}\right)^{1/3}. \tag{7}$$

Similarly, the boundary layer thickness scale δ_B associated with bottom friction is

$$\delta_B = \frac{r}{\beta}, \tag{8}$$

and the scale for the inertial boundary layer δ_I, estimated by GS, is given by

$$\delta_I = \text{Ro}^{2/3} l. \tag{9}$$

where Ro is the final Rossby number. The parameters for the various experiments are listed in Table 1.

a. Experiment I: $\nu = 50 \text{ m}^2 \text{ s}^{-1}$ and $r = 5 \times 10^{-8} \text{ s}^{-1}$

This reference experiment (expt I) was carried out with conventional parameter values for the frictional coefficients. The eddy viscosity is taken as $\nu = 50 \text{ m}^2 \text{ s}^{-1}$ and the bottom friction coefficient as $r = 5 \times 10^{-8} \text{ s}^{-1}$. The resulting time-mean flow patterns are depicted in Fig. 2. In the upper layer (Fig. 2a), the flow is characterized by two gyres, a cyclonic one in the northern part of the domain and an anticyclonic one in the southern part, separated by a meandering jet with intense recirculating regions on both sides. The boundary currents result from the westward intensification of the circulation, with the western wall acting as a source of small-scale energy. When nonlinear effects become important, the boundary layers are not strong enough to dissipate the total input of vorticity to the large-scale flow by the wind (Pedlosky 1987; Cessi et al. 1990). The recirculating gyres flanking the midlatitude jet then act as a dissipation mechanism in which potential vorticity is modified in the compressed streamlines of the gyres (Böning 1986; Cessi 1991; Chassignet 1995).

Inertial recirculating gyres are also generated in the lower layer into which eddy momentum fluxes are transmitted by vortex stretching. A first set of gyres is located in the middle of the domain underneath the upper-layer recirculating gyres, where mesoscale eddies are frequently generated via vortex stretching by meanders of the upper-layer free jet (Figs. 2b,d). The potential vor-
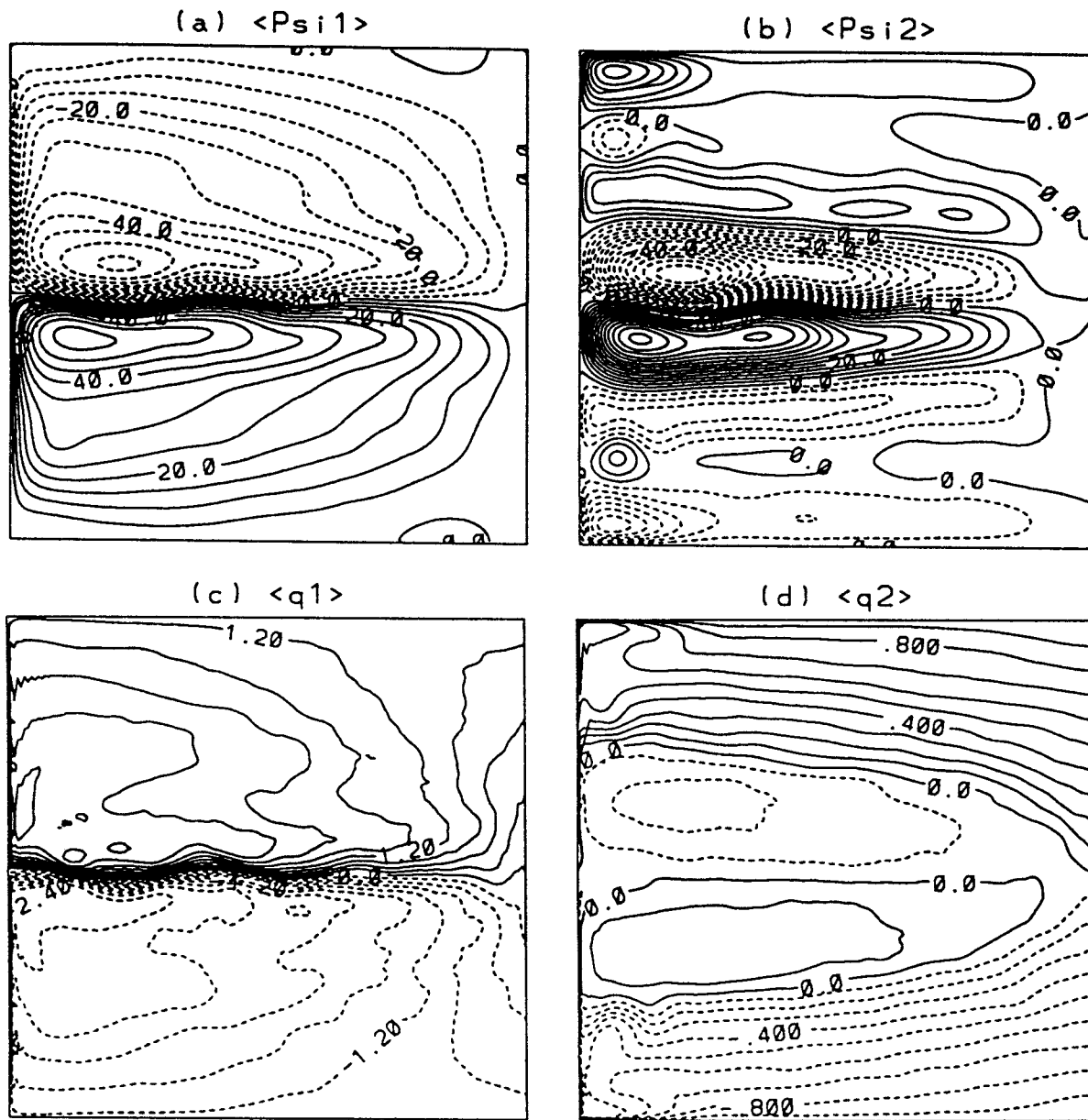
FIG. 2. (a) Upper-layer mean transport streamfunction (CI = 5 Sv), (b) lower-layer mean transport streamfunction (CI = 10 Sv), (c) upper-layer mean potential vorticity (nondimensional; CI corresponds to 0.9×10^{-6} s^{-1}), (d) lower-layer mean potential vorticity (nondimensional; CI corresponds to 2.6×10^{-6} s^{-1}) for expt I.

ticity is homogenized within these gyres in agreement with the theory of Rhines and Young (1982). In both layers, the maximum transport is achieved via these inertial gyres (55 and 73 Sv in the upper and lower layers, respectively). The resulting picture is qualitatively consistent with the scenario presented by Marshall and Nurser (1986) for relatively weak forcing and dissipation.

One should also note the presence in the lower layer of a second set of gyres along the northern and southern boundaries of the domain (Fig. 2b), as these will play a significant role in the overall circulation when dissi-

pation is reduced. These types of gyres are commonly observed in idealized simulations of midlatitude ocean circulation using quasigeostrophic (e.g., Verron and Provost 1991; Barnier et al. 1991) as well as primitive equation models (e.g., Chassignet and Bleck 1993). In the following experiments, it will be shown that, as dissipation is reduced, these gyres will develop into Fofonoff-like gyres and that they will eventually occupy the entire domain.

The energy budget of the reference experiment (expt I) is displayed in Fig. 3. For a detailed explanation of the energetics, the reader is referred to Holland (1978).
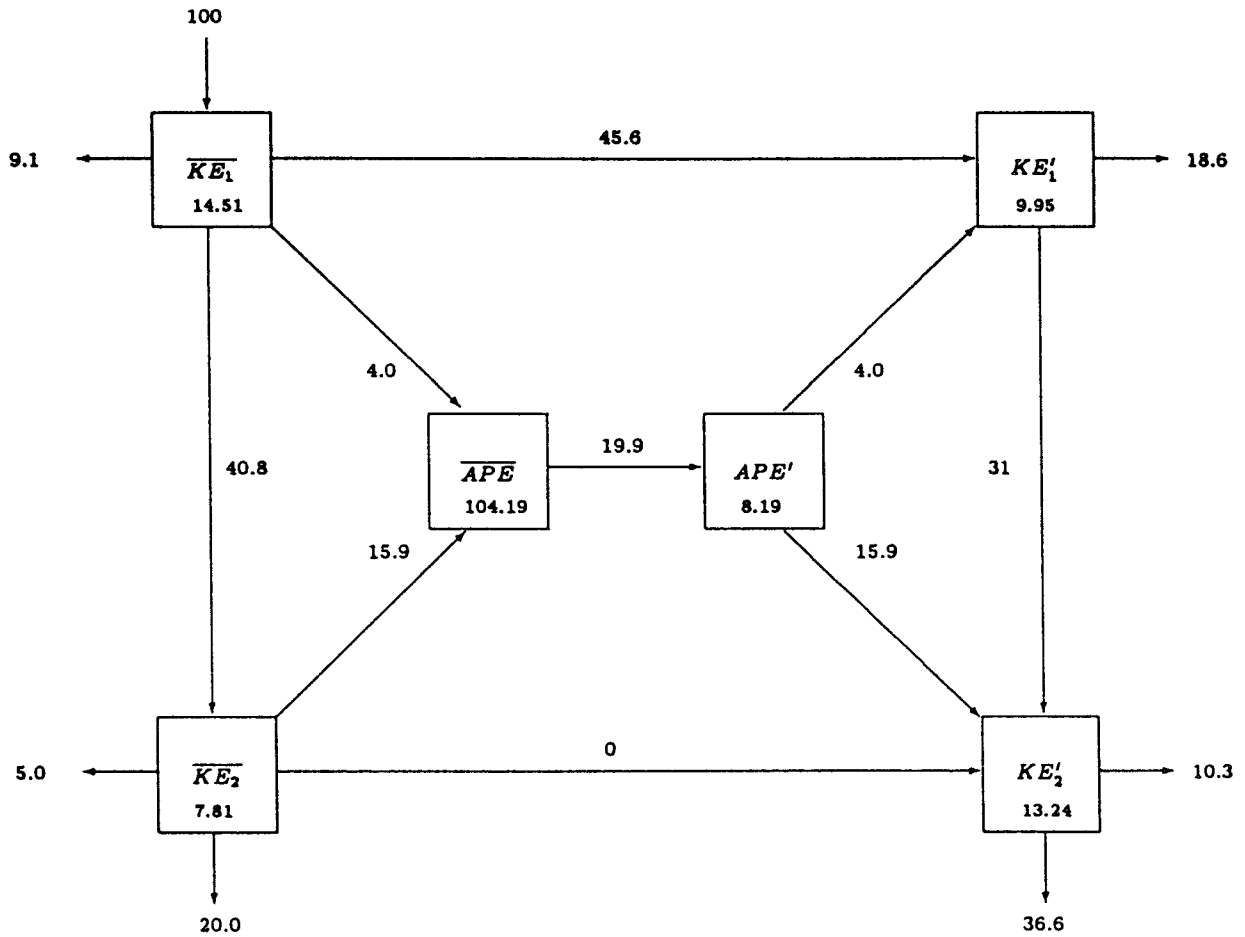
FIG. 3. Energy budget for expt I. The upper portion of the diagram denotes the upper-layer energetics, and the lower portion the lower-layer energetics. The mean and eddy components are displayed on the left- and right-hand side, respectively. The basin-averaged energy totals are shown inside the boxes. The arrows between the boxes indicate internal energy transfer rates associated with baroclinic and barotropic instabilities. The external arrows show the energy input rate by wind forcing and the energy dissipation rates by lateral and bottom friction. Energy transfer rates are expressed in proportion to the wind energy input rate (100%). Wind energy input rate is 3.34×10^{-3} N m^{-1} s^{-1}. Energy unit is 10^3 N m^{-1}. For detailed information about the energetics, the reader is referred to Holland (1978).

Experiment I is characterized by a relatively even distribution of the total kinetic energy between the upper and lower layers, which in turn is roughly equally distributed between the mean and eddy components. The energy input due to the wind is dissipated almost equally by lateral viscosity and by bottom friction. The maximum kinetic energies for each layer are listed in Table 2. For the upper layer, the maximum mean kinetic energy is generated within the narrow western boundary layers and corresponds to a current speed of 1 m s^{-1},

TABLE 2. Maximum kinetic energies (unit: cm^2 s^{-2}) and maximum transports (Sv) in both layers for expts I–IV.

Expt	$\overline{KE}_{1max}$	KE'_{1max}	$\overline{KE}_{2max}$	KE'_{2max}	$\overline{\psi}_{1max}$	$\overline{\psi}_{2max}$
I	5159	1662	337	184	55	83
II	6093	3556	761	443	63	95
III	7421	7826	1839	507	53	122
IV	7060	7274	8284	926	43	364

typical of western boundary currents such as the Florida Current (e.g., Richardson et al. 1969). Not surprisingly, the maximum eddy kinetic energies are found along the meandering midlatitude jet and have the same order of magnitude as in the observations (e.g., Richardson 1983; Thompson and Schmitz 1989, for the Gulf Stream). The simulated flow patterns and the approximate values for transports and kinetic energies place this experiment in a parameter space typical for this kind of idealized numerical simulation (Holland and Schmitz 1985).

b. *Experiment II: $\nu = 1.5$ m^2 s^{-1} and*
   $r = 5 \times 10^{-8}$ s^{-1}

In experiment II, the lateral viscosity coefficient is drastically reduced by a factor of 30 to $\nu = 1.5$ m^2 s^{-1}. As a result, the viscous boundary layer scale δ_L [Eq. (7)] decreases to 4 km from 14 km in experiment I. The
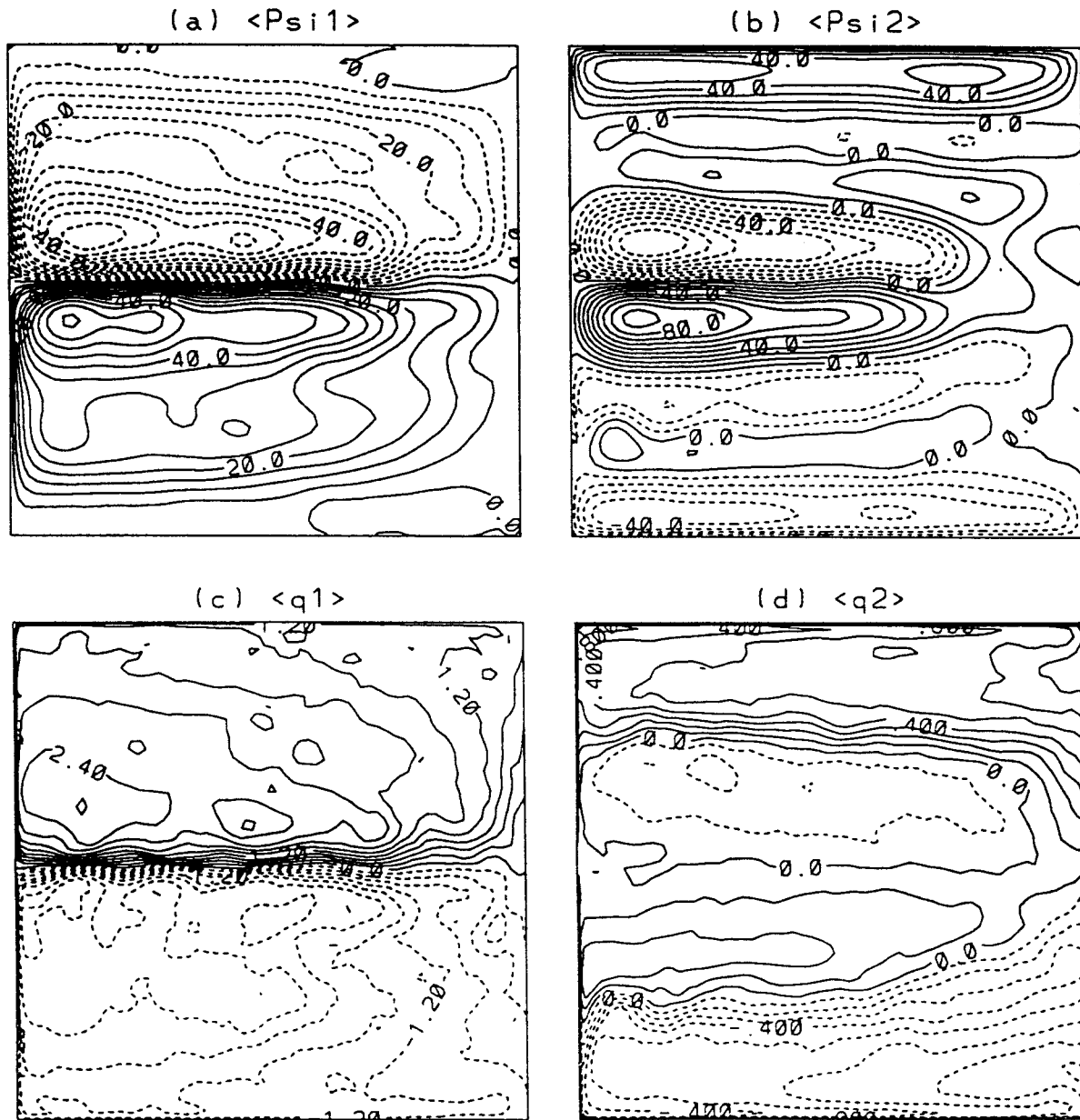
(a) <Psi1>

(b) <Psi2>

(c) <q1>

(d) <q2>

FIG. 4. (a) Upper-layer mean transport streamfunction (CI = 5 Sv), (b) lower-layer mean transport streamfunction (CI = 10 Sv), (c) upper-layer mean potential vorticity (nondimensional; CI corresponds to 0.9×10^{-6} s^{-1}), (d) lower-layer mean potential vorticity (nondimensional; CI corresponds to 2.6×10^{-6} s^{-1}) for expt II.

boundary layer thickness scale δ_B associated with the bottom friction [Eq. (8)] remains constant and is equal to 3 km. These two boundary layers are not resolved in experiment II, even though the resolution in that experiment was increased to a grid spacing of about 7 km (Table 1). Griffa et al. (1996) showed that actually resolving the small viscous boundary layer did not affect the equilibrium flow provided that the inertial boundary layer is resolved. Hence, it is important to resolve the inertial boundary layer $\delta_I \approx 32$ km of experiment II. This is achieved by the chosen grid spacing (Table 1).

The resulting mean flow is illustrated in Fig. 4. While the upper-layer mean streamfunction remains virtually unchanged, the lower layer displays significant modifications. Most notable is the strengthening of the gyres along the southern and northern boundaries of the domain. These gyres now cover the entire zonal extent of the basin (Fig. 4b). The intensity of the inertial recirculating gyres in the middle of the domain also increases, but the gyres themselves do not extend across the entire basin. Their zonal extent is determined by the balance between the tendency for the highly inertial
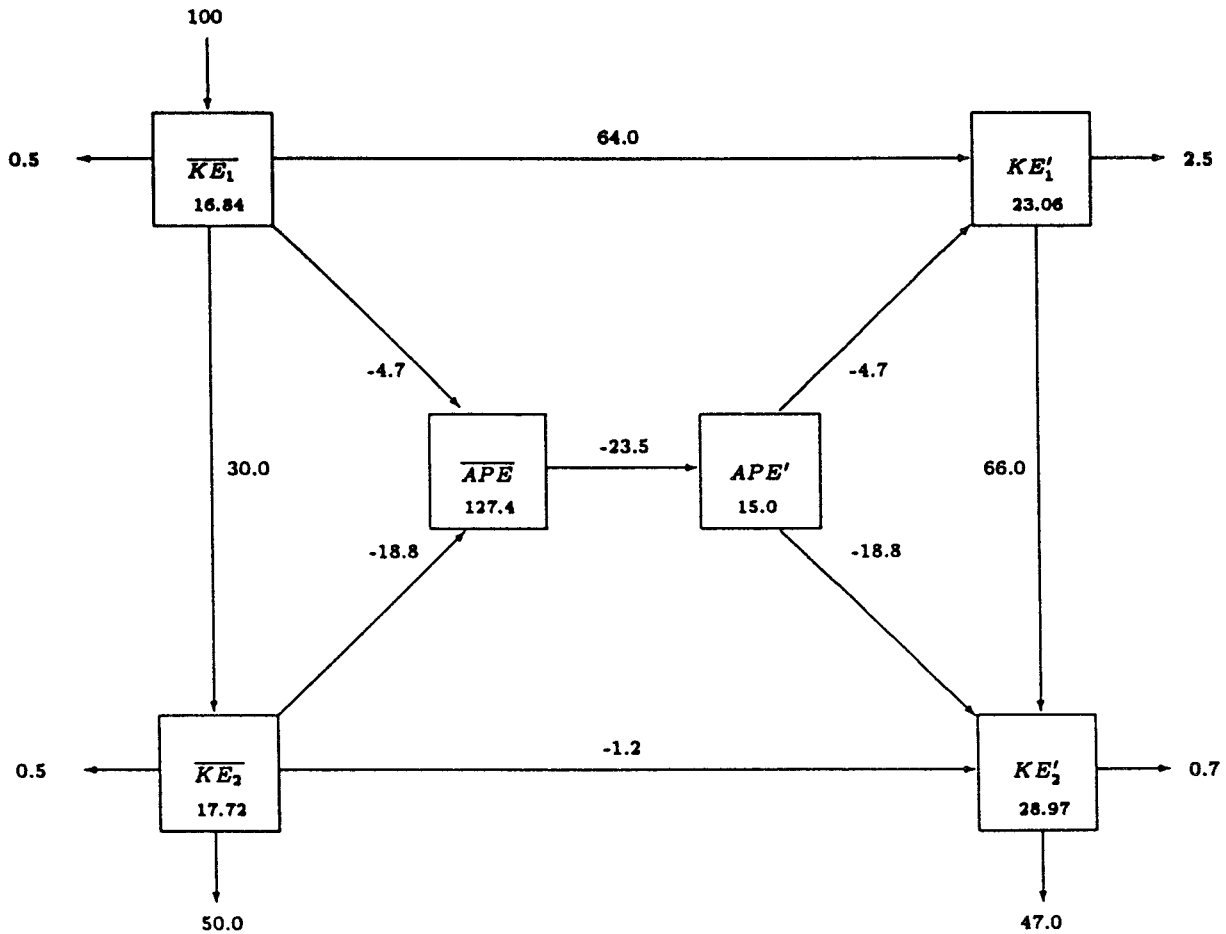
FIG. 5. Energy budget for expt II. Wind energy input rate is 3.39×10^{-3} N m^{-1} s^{-1}. Energy unit is 10^3 N m^{-1}.

mid-latitude jet to extend all the way across the basin and its inherent instability, which generates mesoscale eddies that disrupt the jet, thereby restricting its zonal penetration (Holland and Schmitz 1985). Both gyre systems exhibit a tendency toward homogenization of potential vorticity inside the gyres (Fig. 4d).

The "original" Fofonoff flows (Fig. 1a), obtained for a barotrophic configuration, assume a linear relation between the potential vorticity q and the streamfunction ψ, $q = c_1\psi + c_2$ with $c_1 > 0$. The Fofonoff solution was generalized by Marshall and Nurser (1986) to stratified flows with weak forcing and dissipation. They showed that solutions satisfying the relationship $q = c_1\psi + c_2$ with $c_1 < 0$ can actually exist in the upper layer, provided that vortex stretching is strong enough. These solutions have two recirculating gyres, separated by an inertial jet, that correspond to the prescribed wind forcing (cyclonic in the north and anticyclonic in the south) (Fig. 1b). These gyres are of opposite sign from those in the "barotropic case." The lower-layer potential vorticity fields are homogenized.

Both types of gyres are present in experiments I and II and both increased in strength when viscosity was

reduced (Fig. 4b). The question then arises as to which system of gyres will eventually dominate the lower-layer circulation. Marshall and Nurser's (1986) solution was derived for weakly forced and dissipative stratified flows. Equilibrium statistical mechanics indicates that Fofonoff-like gyres (i.e., circulation in the same direction as the conventional barotropic Fofonoff flow) should be the *stable* solutions toward which the nonlinear terms tend to drive the system (SHH). We therefore anticipate that those gyres, which tend to become more dominant as the nonlinearity in the system increases (i.e., as the friction decreases), will be associated with Fofonoff flows.

The energy budget of experiment II is shown in Fig. 5. There is a significant increase in the eddy kinetic energy levels in both layers, as well as in the mean kinetic energy of the lower layer, when compared to experiment I. This corresponds to a more efficient use of the wind torque in order to reach a higher energy level and strongly indicates an increase in the nonlinearity of the system. Finally, most of the energy dissipation now takes place in the lower layer via the bot-

(a) <Psi1>
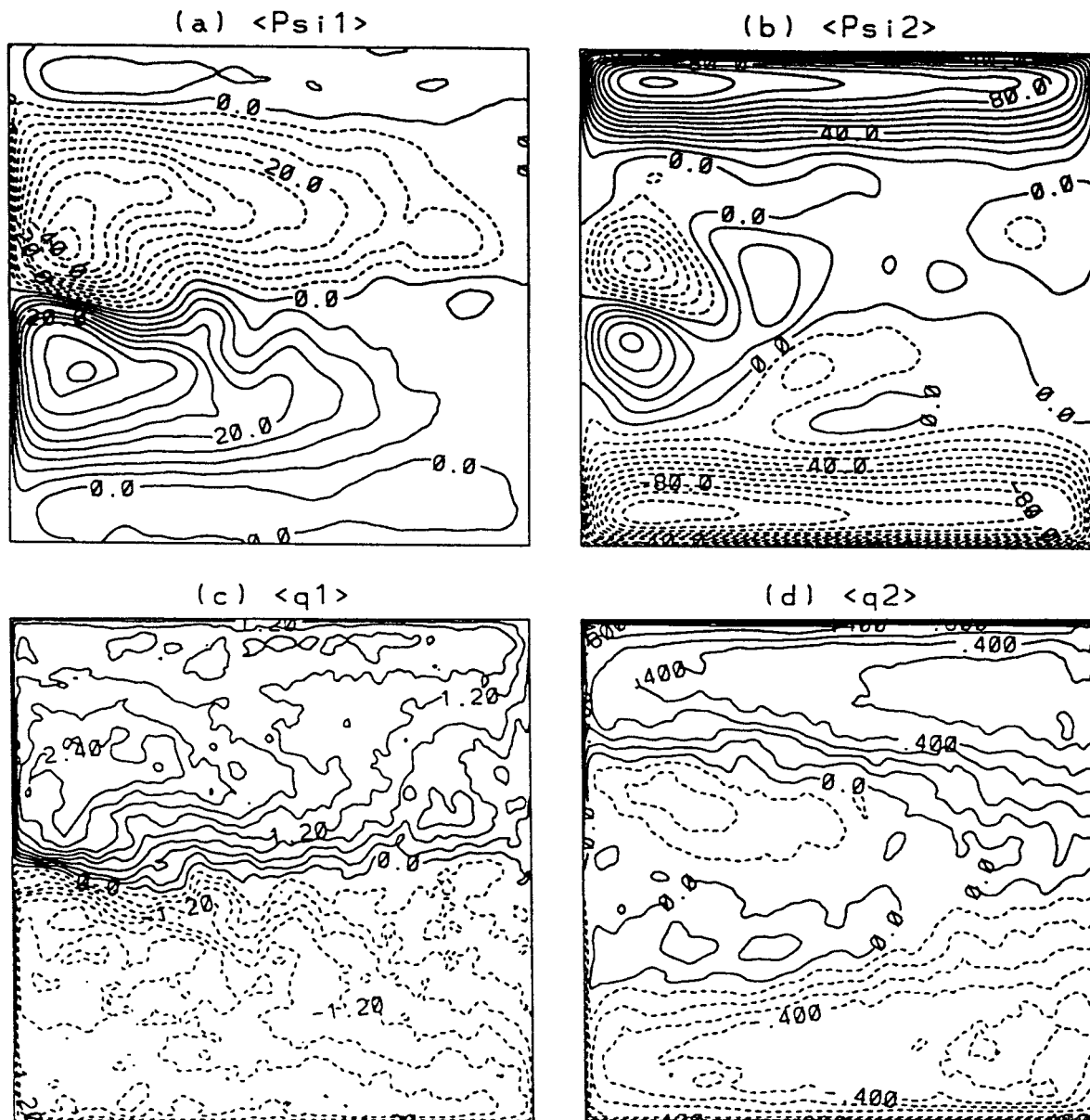
(b) <Psi2>

(c) <q1>

(d) <q2>

FIG. 6. (a) Upper-layer mean transport streamfunction (CI = 5 Sv), (b) lower-layer mean transport streamfunction (CI = 10 Sv), (c) upper-layer mean potential vorticity (nondimensional; CI corresponds to 0.9×10^{-6} s^{-1}), (d) lower-layer mean potential vorticity (nondimensional; CI corresponds to 2.6×10^{-6} s^{-1}) for expt III.

tom friction, shared equally between mean- and eddy-flow activity.

c. Experiment III: $\nu = 0$ and $r = 5 \times 10^{-8}$ s^{-1}

In a further deviation from the parameter space used in typical midlatitude ocean simulations, the lateral viscosity coefficient in this experiment is set to zero. This has a strong dynamical influence on the solution, as shown by the mean fields displayed in Fig. 6. This sensitivity of the solution to a small change in lateral vis-

cosity also indicates that the dissipation associated with the model's numerics is minimal.

The primary difference from experiment II is in the disintegration of the midlatitude jet in the mean field and the accompanying recirculation gyres in both layers (Figs. 6a,b). The convergence of the western boundary currents still generates a midlatitude jet; however, its fluctuations are so violent that the resulting mean signature is weak. Consequently, the maximum upper-layer eddy kinetic energy is higher than in experiment II and is nearly five times that of experiment I (Table 2). This
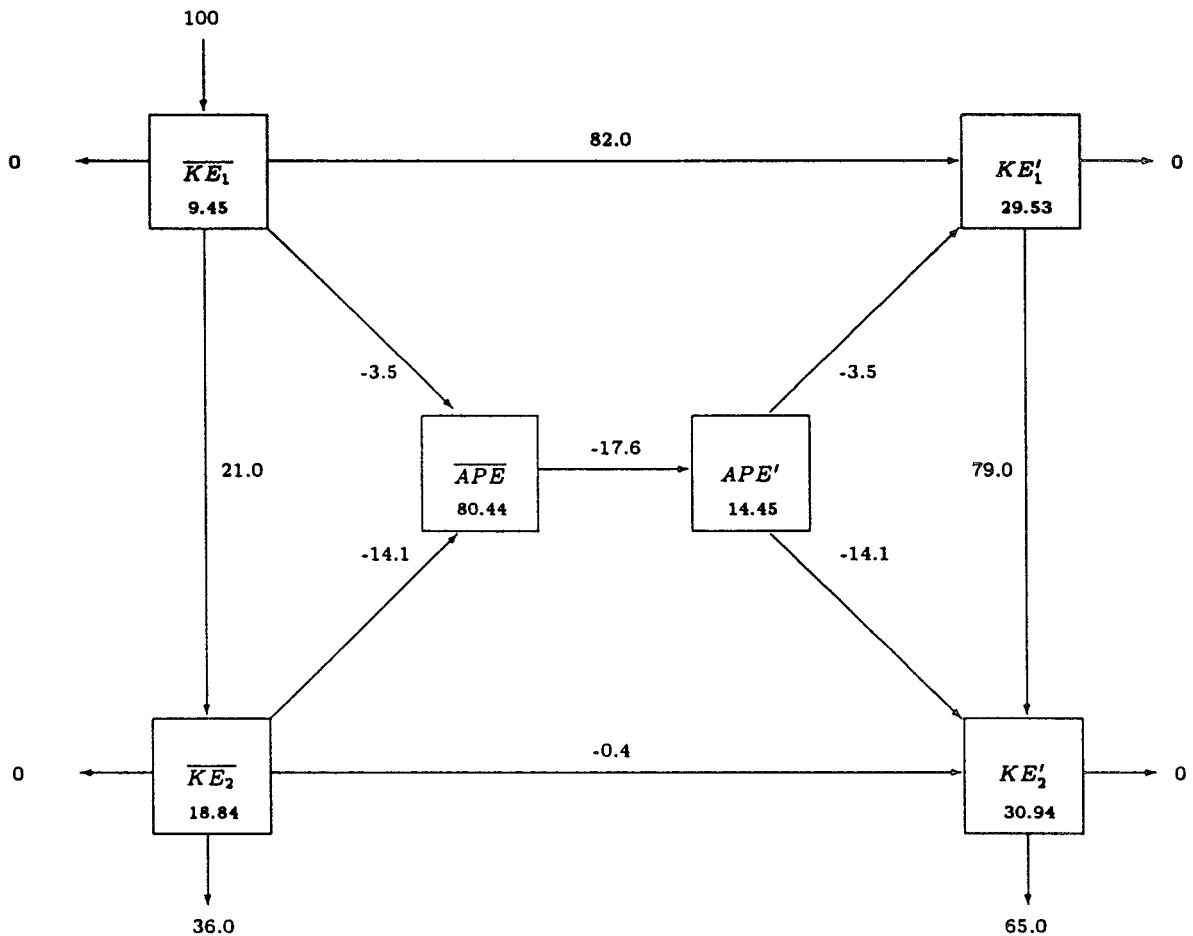
FIG. 7. Energy budget for expt III. Wind energy input rate is 2.37×10^{-3} N m^{-1} s^{-1}. Energy unit is 10^3 N m^{-1}.

result illustrates that midocean recirculating gyres are *not stable* for very small values of eddy viscosity.

In the lower layer, the northern and southern boundary gyres are now dominant and gained strength as the dissipation is reduced, in agreement with the characteristics of Fofonoff flows given by the equilibrium mechanics theory. In experiment III, each of these gyres now transports more than 120 Sv (Table 2) and displays the highest mean kinetic energy. These gyres significantly influence the upper-layer flow as their signature is visible in Fig. 6a.

Potential vorticity is mixed and homogenized in these bottom layer gyres (Fig. 6d). Homogenization of potential vorticity is commonly observed in numerical experiments, where the dissipation operator and associated boundary conditions induce deviations from the ideal unforced–undamped system, for which the equilibrium statistical mechanics theory (SHH) predicts a linear relationship between the streamfunction and potential vorticity. Cummings (1992) found that the boundary conditions can have a global influence on the realization of the equilibrium state and, in particular, that the free-slip conditions may lead to the homogenization of potential

vorticity within the recirculating flow. Cummings employed the theory of Rhines and Young (1982) to explain how homogenization takes place. This theory assumes that the mixing induced by eddies can be parameterized as $\overline{\mathbf{u}'q'} = -\kappa\nabla\overline{q}$, where κ is a diffusivity coefficient. When the influence of friction is small in comparison to that of the eddies, Rhines and Young (1982) proved that within the time-averaged closed contours of the streamfunction, the potential vorticity is nearly uniform. Wang and Vallis (1994) stated that the viscous dissipation appears to drive the potential vorticity field toward homogenization, but they also argued that the detailed form of the viscosity operator is less important than the boundary conditions. Griffa et al. (1996) stated that friction tends to flatten the slope of the streamfunction–potential vorticity curve. In this experiment (expt III), the free-slip boundary condition is effective via the numerical implementation of the nonlinear advective terms.

The energy budget (Fig. 7) remains qualitatively the same as in experiment II. The significant loss of the mean available potential energy is due to the disappearance of the midocean recirculating gyres.

(a) <Psi1>
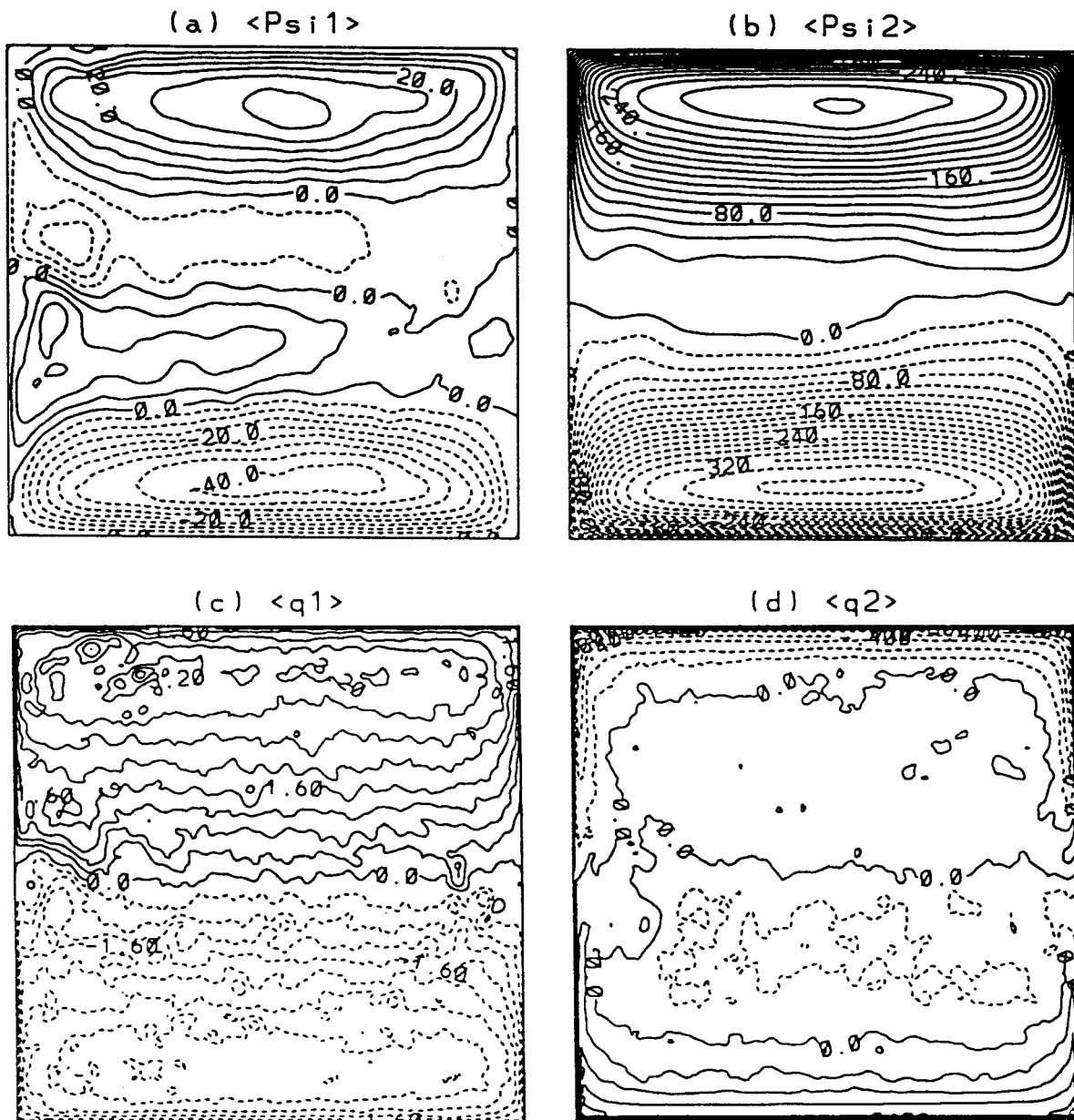
(b) <Psi2>

(c) <q1>

(d) <q2>

FIG. 8. (a) Upper-layer mean transport streamfunction (CI = 5 Sv), (b) lower-layer mean transport streamfunction (CI = 20 Sv), (c) upper-layer mean potential vorticity (nondimensional; CI corresponds to 1.2×10^{-6} s^{-1}), (d) lower-layer mean potential vorticity (nondimensional; CI corresponds to 2.6×10^{-6} s^{-1}) for expt IV.

d. Experiment IV: $\nu = 0$ and $r = 10^{-9}$ s^{-1}

In experiment IV, the bottom friction coefficient is reduced to $r = 10^{-9}$ s^{-1}, which corresponds to a damping timescale of approximately 30 yr. The model is integrated for an additional 27 years starting from the statistical steady state of experiment III, and the statistics are computed over the final 7 years. At the end of the integration, the energetics indicate that the system is fairly close to a statistical steady state but is still slowly evolving. The trend during the last 7 years of

the integration is small enough for the mean flow pattern to be representative.

The mean flow patterns are displayed in Fig. 8. In the lower layer, Fofonoff-like inertial gyres now completely dominate the solution and occupy the entire domain (Fig. 8b). The transport associated with these gyres exceeds 300 Sv and their signature is clearly dominant in the upper layer (Fig. 8a). The configuration in this layer indicates a tendency for the solution to barotropize, but the upper-layer transports are smaller by almost an order of magnitude when compared to the lower-layer
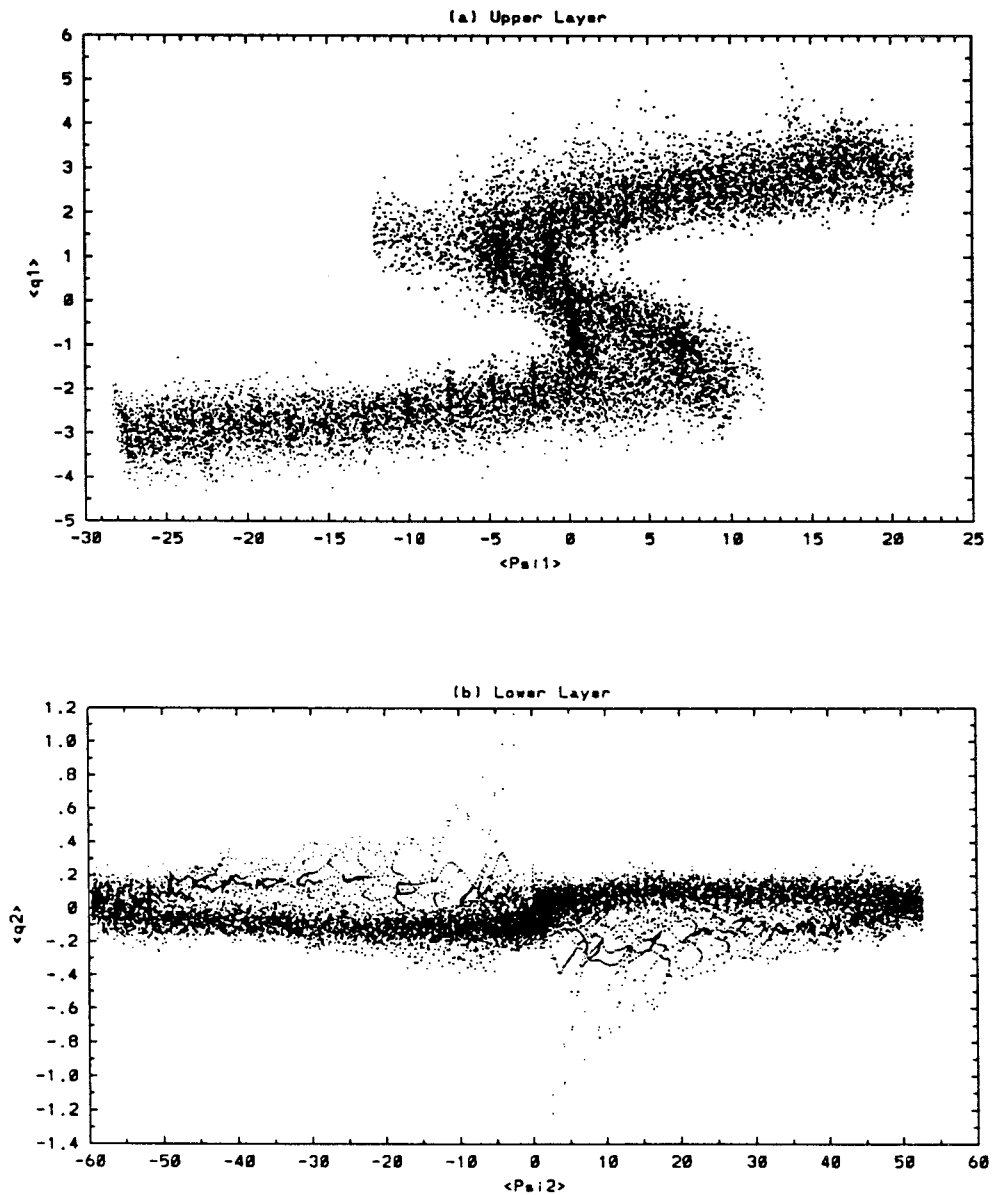
FIG. 9. Scatterplot of mean streamfunction versus potential vorticity (nondimensional) for expt IV (a) in the upper layer and (b) in the lower layer.

transports (Table 2). A fully barotropic solution would exhibit transports in proportion to the upper/lower layer thickness ratio, namely 1/4 for this set of experiments. The resistance of the solution to complete barotropization is the result of the wind forcing acting in the upper layer in opposition to the Fofonoff flows (see section 4f for a detailed discussion). As discussed by GS, this type of wind forcing can completely prohibit the emergence of Fofonoff flows in a barotropic model. In this two-layer model, however, Fofonoff-like gyres emerge, by first appearing in the lower layer to eventually dominate the whole water column. The wind-driven gyres are still apparent in the instantaneous up-

per-layer flow fields, but the mean component is weak due to a strong fluctuation field (see the eddy kinetic energy values listed in Table 2).

The resemblance of this solution to the Fofonoff solution can be further quantified by a scatterplot of the mean streamfunction and potential vorticity in both layers (Fig. 9). Despite the large amount of noise due to the variability, the northern and southern upper-layer inertial gyres are characterized by a linear relationship between the streamfunction and potential vorticity. The two gyres are separated by the wind-driven region in the middle of the domain, where potential vorticity increases with latitude (i.e., the negatively sloped region
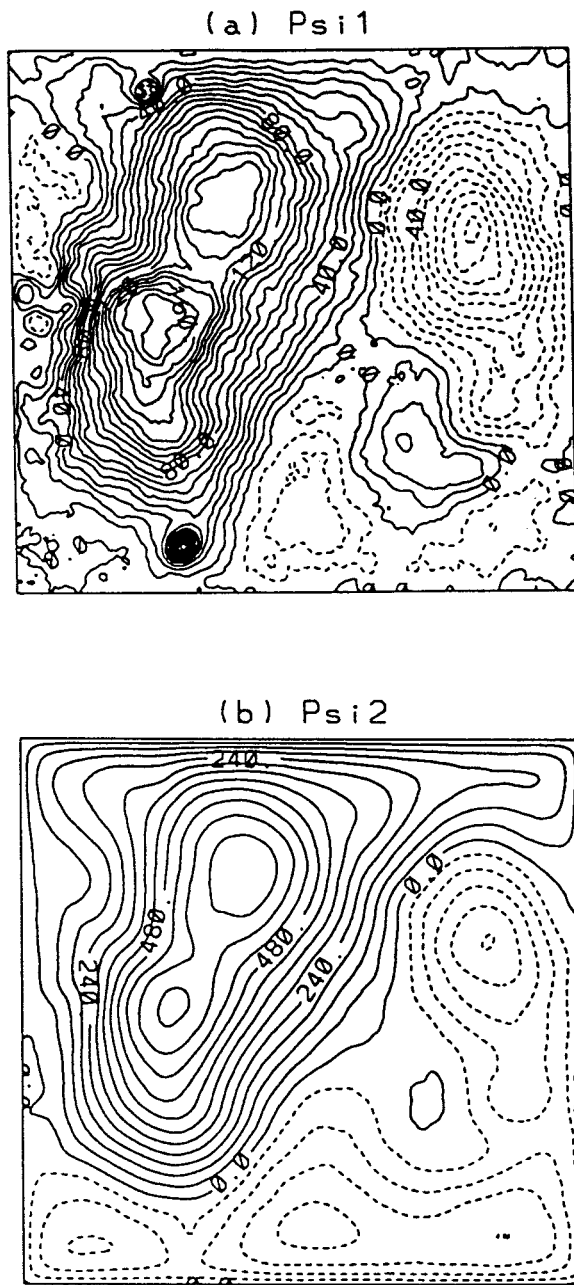
(a) Psi 1

(b) Psi 2

FIG. 10. Instantaneous streamfunctions of expt IV at the end of the integration for (a) upper layer (CI = 10 Sv) and (b) lower layer (CI = 60 Sv).

TABLE 3. Seven-year averaged energy for expt IV (unit: 10^3 N m^{-1}).

Energy totals	
$\overline{KE}_1$	14
$\overline{KE}_2$	129
KE'_1	60
KE'_2	100
$\overline{APE}$	200
APE'	12

ory, that the equilibrium flow is nearly barotropic at scales of motion larger than the radius of deformation, while at smaller scales the streamfunctions in the two layers should be statistically uncorrelated.

The energy budget for this experiment is not in balance since the solution did not reach a statistical steady state and is therefore not presented. However, for the purpose of completeness and comparison, the basin-averaged kinetic and potential energies over the final 7 years of integration are given in Table 3. Both the lower-layer kinetic energy and available potential energy increased by a factor of 5 when compared to those of experiment III.

e. Experiment V: $\nu = 0$ and $r = 5 \times 10^{-4}$ s^{-1}

The four experiments presented in the previous subsections appear to indicate the flow tendency toward a Fofonoff regime in a two-layer quasigeostrophic model, despite the fact that the wind forcing acted to oppose this regime (see section 4f for a detailed discussion). This result was achieved with very small dissipation in the system and conforms well with the assumptions of theoretical models (SHH). Intuitively, one would not expect a Fofonoff-like solution with high dissipation. This is, however, not necessarily always the case as illustrated by the experiment presented in this section. As before, stratification plays an important role in the behavior of the system and leads to an unexpected result.

Experiment V was performed with a high bottom friction coefficient, $r = 5 \times 10^{-4}$ s^{-1} (10 000 times greater than in expt IV). This coefficient corresponds to a damping timescale of about 33 min and clearly lies outside the realistic parameter regime of any oceanic application. However, the purpose of this study is to explore the emergence of Fofonoff-like solutions over the full extent of the parameter space. Due to reasons associated with the sequence of the experiments conducted during the research phase, the domain size in experiment V is 3500 km as opposed to 2000 km in the previous experiments. The net effect is a modification of the final Rossby number (see Table 1), which controls the intensity and size of the inertial recirculations. It was not deemed necessary to repeat this experiment in the smaller domain.

In experiment V, the lateral viscosity is gradually re-

in Fig. 9a). In the lower layer, instead, the potential vorticity is strongly homogenized (Fig. 9b).

A sample of experiment IV instantaneous streamfunctions is presented in Fig. 10. Even though both layers are in general agreement on the large scale, the upper layer exhibits a significant amount of small-scale activity (i.e., at scales smaller than the radius of deformation), which is absent in the lower-layer flow. This feature is consistent with the conclusions reached by SHH, based on the equilibrium statistical mechanics the-

duced to zero during the time span of the integration. As the lateral viscosity is decreased, the upper layer dissipates less and less energy and becomes very energetic. The lower layer then basically acts as a sink of energy and displays only a very weak flow because of the high damping. Note that this case is inherently different from a reduced gravity model, where the lower layer is motionless and hence cannot dissipate energy.

The reduction of the lateral viscosity coefficient has a significant impact on the separation point of the midlatitude jet. In the high-viscosity regime, the western boundary layers are frictional and do not display high variability. As the viscosity is reduced, the viscous boundary layer thickness becomes smaller than the inertial boundary layer thickness, and the boundary layer dynamics becomes controlled by a balance between the inertial terms and the beta effect. The separation point (i.e., where the boundary currents turn eastward) is governed by fully nonlinear dynamics (e.g., Harrison and Holland 1981), in which the eddy component of the advective term balances its mean component [i.e., $J(\overline{\psi}, \nabla^2\overline{\psi}) \approx \overline{J(\psi', \nabla^2\psi')}$]. In the absence of strong damping in the boundary layer, the separation point becomes highly variable and boundary eddies are generated. This process is illustrated by a series of instantaneous upper-layer streamfunction contour diagrams in Fig. 11. Initially (at $t = t1$), the midlatitude jet separates near the zero wind-stress curl line (ZWCL). The separation point is highly variable, and the northward-flowing boundary current overshoots the ZWCL by approximately 1300 km before it sheds a boundary eddy ($t = t2$ and $t = t3$) and begins to retract. These eddies tend to accumulate along the northern and southern boundaries and travel eastward with an approximate speed of 10 cm s^{-1} until they interact with other eddies that migrate westward with a speed of 1 cm s^{-1}, which corresponds to the typical long Rossby wave speed ($t = t4$ and $t = t5$).

As the lateral viscosity becomes smaller, the jet becomes more energetic and possesses a very weak mean flow. The eddy generation near the separation latitude increases, and the migration of eddies along the zonal boundaries tends to mix the potential vorticity. The upper and lower mean streamfunctions corresponding to the end result, namely, zero lateral viscosity, are shown in Fig. 12. The lower-layer flow is of course very weak [$O(10^{-2})$ Sv] and does not exhibit a dominant mean flow (although it displays a pattern of waves). In the upper layer, on the other hand, the wind-forced interior is visible, but its mean component is weak because of the strong fluctuations. The most prominent features are the recirculating gyres along the southern and northern boundaries, whose sense of direction is consistent with Fofonoff flows. Note that these gyres appear exclusively in the upper layer despite the fact that the wind forcing acts in opposition to their direction of flow.

In contrast to experiment IV in which the Fofonoff-like gyres were strongly barotropic, the gyres in experiment V are mostly baroclinic. In order to develop the large transports observed in these gyres (which exceed 180 Sv), the density interface must stretch by an amount comparable to its initial thickness, hence violating the quasigeostrophic approximation. However, the tendency toward this flow pattern was clearly observed within the quasigeostrophic range while the lateral viscosity was gradually reduced during the integration. The flow presented in Fig. 12a is representative of the equilibrium solution for this parameter regime.

In order to quantify the proximity of this solution to Fofonoff flows, the relationship between the streamfunction and potential vorticity is investigated. The upper-layer mean potential vorticity is plotted in Fig. 12c. There is a strong correspondence between the streamfunction and the potential vorticity in the upper layer, as illustrated by the scatterplot of Fig. 13, which shows a linear relationship between the streamfunction and the potential vorticity. This can be explained by considering the characteristics of this experiment and the definition of the upper-layer vorticity [Eq. (3)]. The respective contributions of the relative vorticity, of the stretching term, and of the beta term are illustrated in Fig. 14. Figure 14a shows the contribution of the stretching term only. Figure 14b shows the contribution of the stretching term and of the beta term combined. The contribution of the relative vorticity is negligible as shown by the near-identity of Fig. 14b and Fig. 13. This is not surprising since F (the Froude number) is much larger than R (the Rossby number) in this experiment [$F/R = (l/R_d)^2$]. While the inclusion of the beta term does modify the $\overline{\psi_1}-\overline{q_1}$ curve in Fig. 14b from that in Fig. 14a, the linear relationship between the streamfunction and potential vorticity in the upper layer is predominantly determined by the stretching term. The linear relationship is then explained by considering that the lower-layer mean flow is virtually nonexistent ($\overline{\psi_1} \gg \overline{\psi_2}$) and that the upper-layer potential vorticity equation reduces to $\overline{q_1} \approx -\delta^{-1}F\overline{\psi_1}$. The slope of the $\overline{\psi_1} - \overline{q_1}$ curve in Fig. 13 is roughly consistent with this relationship ($F = 8.5 \times 10^{-3}$, $\delta = 0.2$ for expt V)

In this section, it has been shown that Fofonoff-like flows are not constrained to unforced–nondissipative regimes, but can also emerge in a regime with unfavorable forcing and high damping, as long as stratification is included in the dynamics.

f. Experiments VI and VII: Reversed wind forcing

In sections 4d and 4e, it is argued that a flow tendency toward a Fofonoff regime can be achieved in a two-layer quasigeostrophic model despite the fact that the wind forcing acted to oppose this regime. In order to substantiate this hypothesis, experiments III and V were repeated with a reversed wind forcing (as expts VI and VII, respectively). With such forcing, the emergence of Fofonoff flows should be favored, and the gyres appearing in the previous experiments should strengthen
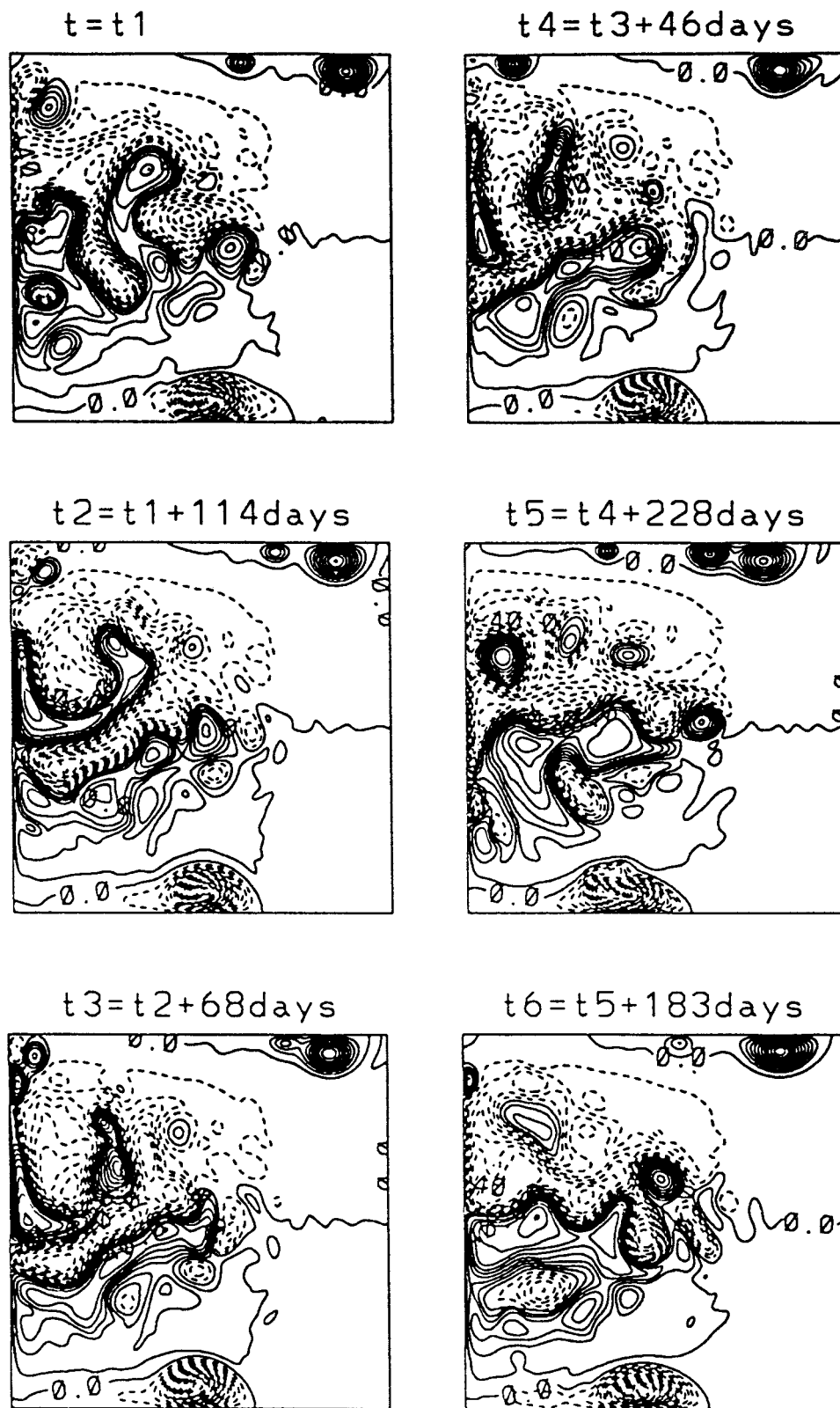
t = t1

t4 = t3 + 46 days

t2 = t1 + 114 days

t5 = t4 + 228 days

t3 = t2 + 68 days

t6 = t5 + 183 days

FIG. 11. Time series of instantaneous upper-layer streamfunctions during spinup phase for expt V (CI = 10 Sv).
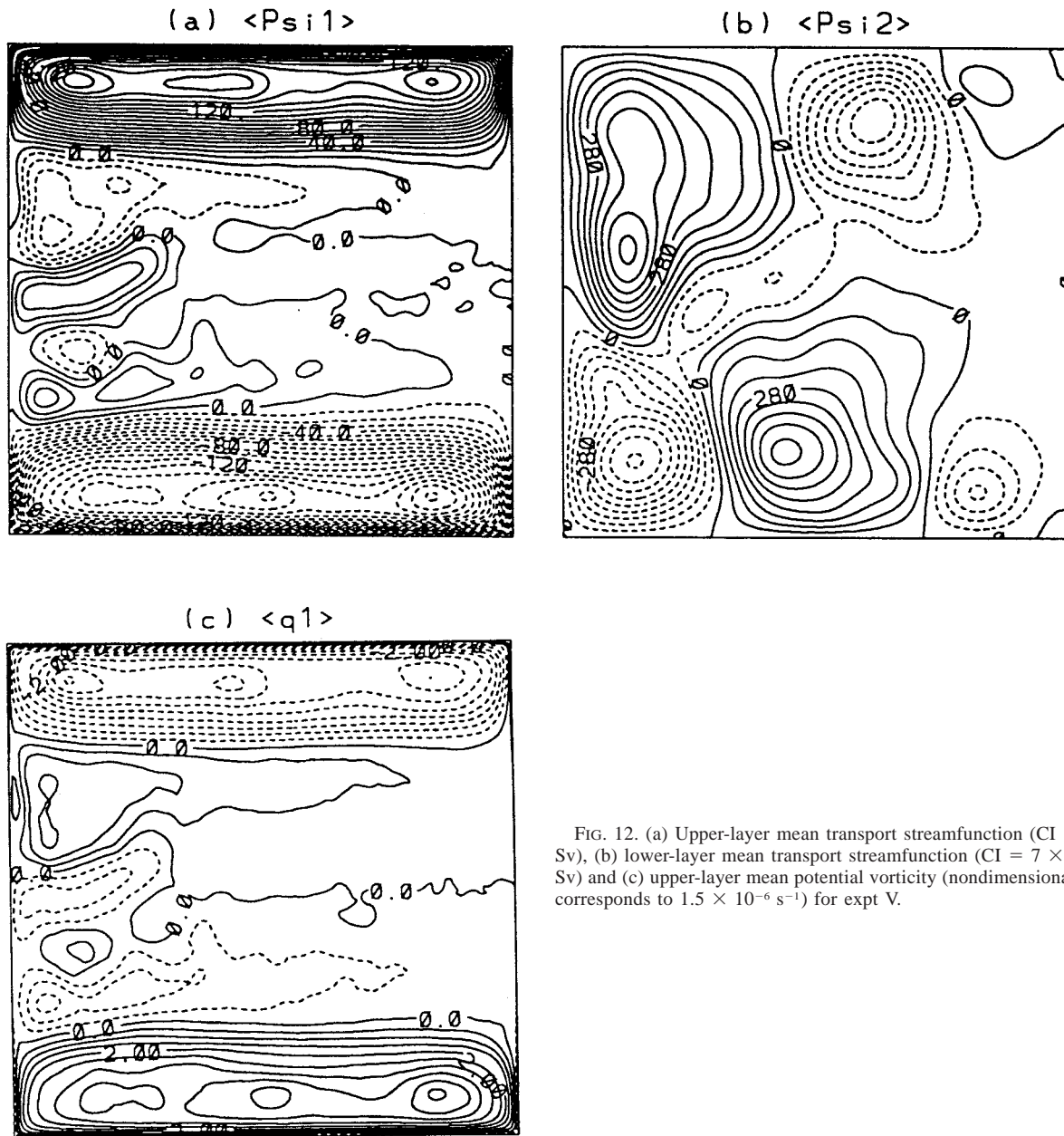
(a) <Psi1>

(b) <Psi2>

(c) <q1>

FIG. 12. (a) Upper-layer mean transport streamfunction (CI = 10 Sv), (b) lower-layer mean transport streamfunction (CI = 7×10^{-3} Sv) and (c) upper-layer mean potential vorticity (nondimensional; CI corresponds to 1.5×10^{-6} s^{-1}) for expt V.

substantially if they are consistent with Fofonoff flows. Griffa and Salmon (1989) demonstrated that in a barotropic quasigeostrophic model the emergence of Fofonoff flows depends strongly on the geometry of the wind stress. In order to reach an equilibrium state, the parameters of experiment III were chosen for experiment VI. The Ekman pumping for both experiments VI and VII is

$$w_E(y) = -W \sin\left(2\pi\frac{y}{l}\right) \quad \text{with} \quad -\frac{l}{2} \le y \le \frac{l}{2}, \quad (10)$$

where the amplitude W remains unchanged from ex-

periments III and V. This forcing drives an anticyclonic gyre in the northern half of the domain and a cyclonic gyre in the southern half.

The mean flows for experiment VI are shown in Fig. 15. A substantial strengthening of the inertial gyres with respect to those in experiment III (Fig. 6) is observed and the scatterplots between the streamfunction and potential vorticity exhibit quasi-linear relationships for both layers (Fig. 16). The slopes are negative and positive in the upper and lower layers, respectively. This is in apparent contrast with experiment IV (Fig. 9) in which the slopes are positive and zero in the upper and lower layers, respectively. The question as to whether
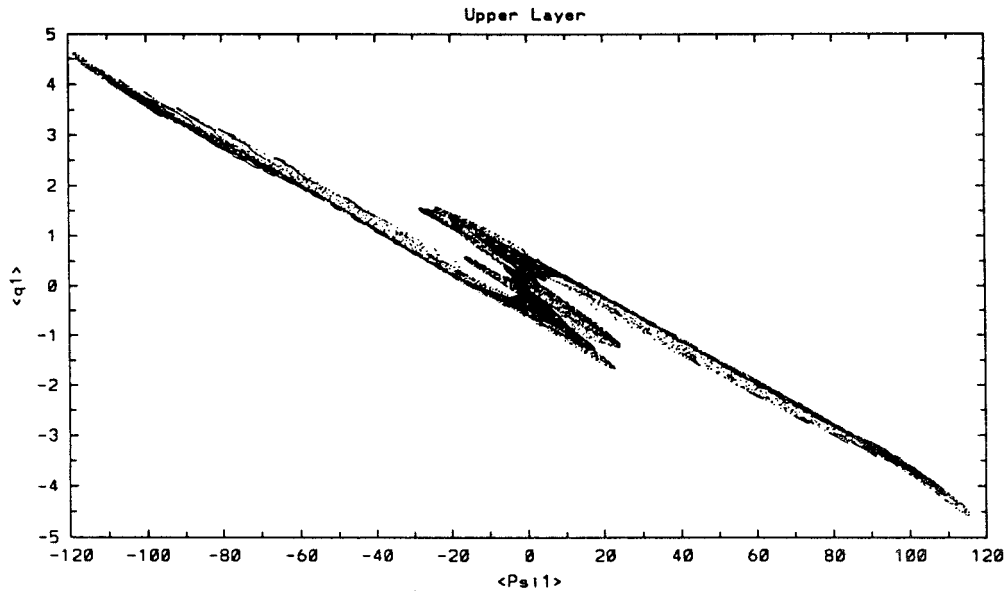
FIG. 13. Scatterplot of mean streamfunction versus potential vorticity (nondimensional) in the upper layer for expt V.

or not these slopes correspond to a Fofonoff regime is discussed in detail in the next section.

The mean flows for experiment VII are illustrated in Fig. 17. Again, the Fofonoff-like gyres strengthen with respect to those in the experiment with unfavorable wind forcing (expt V, Fig. 12), and the gyres occupy the entire upper layer. The lower-layer flow is, as in experiment V, very weak due to high bottom friction. The scatterplot between the upper-layer streamfunction and potential vorticity shows a linear relationship (Fig. 18). As in experiment V, the slope is negative and its value is predominantly determined by the stretching term.

The results of both experiments show that the inertial gyres intensify substantially when the wind forcing is favorable. The gyres in experiments III–VII all display a quasi-linear relationship between the mean streamfunction and potential vorticity. However, these relationships exhibit a variety of slopes, which can be negative, zero, or positive in each layer. The consistency of these slopes with the nature of Fofonoff gyres is discussed in the following section.

5. Discussion

Fofonoff flows are defined by a linear relationship between the streamfunction and potential vorticity. Classical Fofonoff gyres (Fofonoff 1954) are defined for a barotropic flow, and the nature of the relationship between the streamfunction and potential vorticity may vary in a model that includes stratification. The experiments presented in section 4 exhibit inertial gyres that have visual resemblance to the classic Fofonoff gyres. However, while the quasi-linear relationship between the streamfunction and potential vorticity is retained in the scatterplots, the corresponding slopes can be posi-

tive, zero, or negative. In this section, we investigate under which conditions Fofonoff flows can exist in a two-layer quasigeostrophic model and we examine the consistency of the gyres discussed in section 4 with Fofonoff flows.

In a barotropic model, assuming the existence of Fofonoff flows, the relationship between the time-averaged potential vorticity and streamfunction can be written as (dropping the superscript for simplicity)

$$q = R\nabla^2\psi + y = c_1\psi + c_2, \qquad (11)$$

For a small Rossby number R, the inertial effects are confined to the boundary layers, and the interior solution is $\psi^i(y) = (y - c_2)/c_1$. The corresponding interior zonal velocity is then $U^i = -d\psi^i/dy = -1/c_1$. In order for the interior flow to be westward ($U^i < 0$), in agreement with Fofonoff flows, c_1 must be positive. Zero or negative slopes are not allowed in a barotropic model.

In a two-layer model, assuming again the existence of Fofonoff flows, the relationships for the mean flows in the upper and lower layers can be written as

$$q_1 = R\nabla^2\psi_1 + y + \frac{F}{\delta}(\psi_2 - \psi_1) = c_1\psi_1 + c_2, \qquad (12)$$

$$q_2 = R\nabla^2\psi_2 + y + \frac{F}{1 - \delta}(\psi_1 - \psi_2) = d_1\psi_2 + d_2. \qquad (13)$$

In the interior, the relative vorticity is small, and the streamfunctions can be expressed as

$$\psi_1^i(y) = \frac{1}{\det}\left(-\frac{F}{1 - \delta}c_2 - c_2d_1 - \frac{F}{\delta}d_2\right.$$
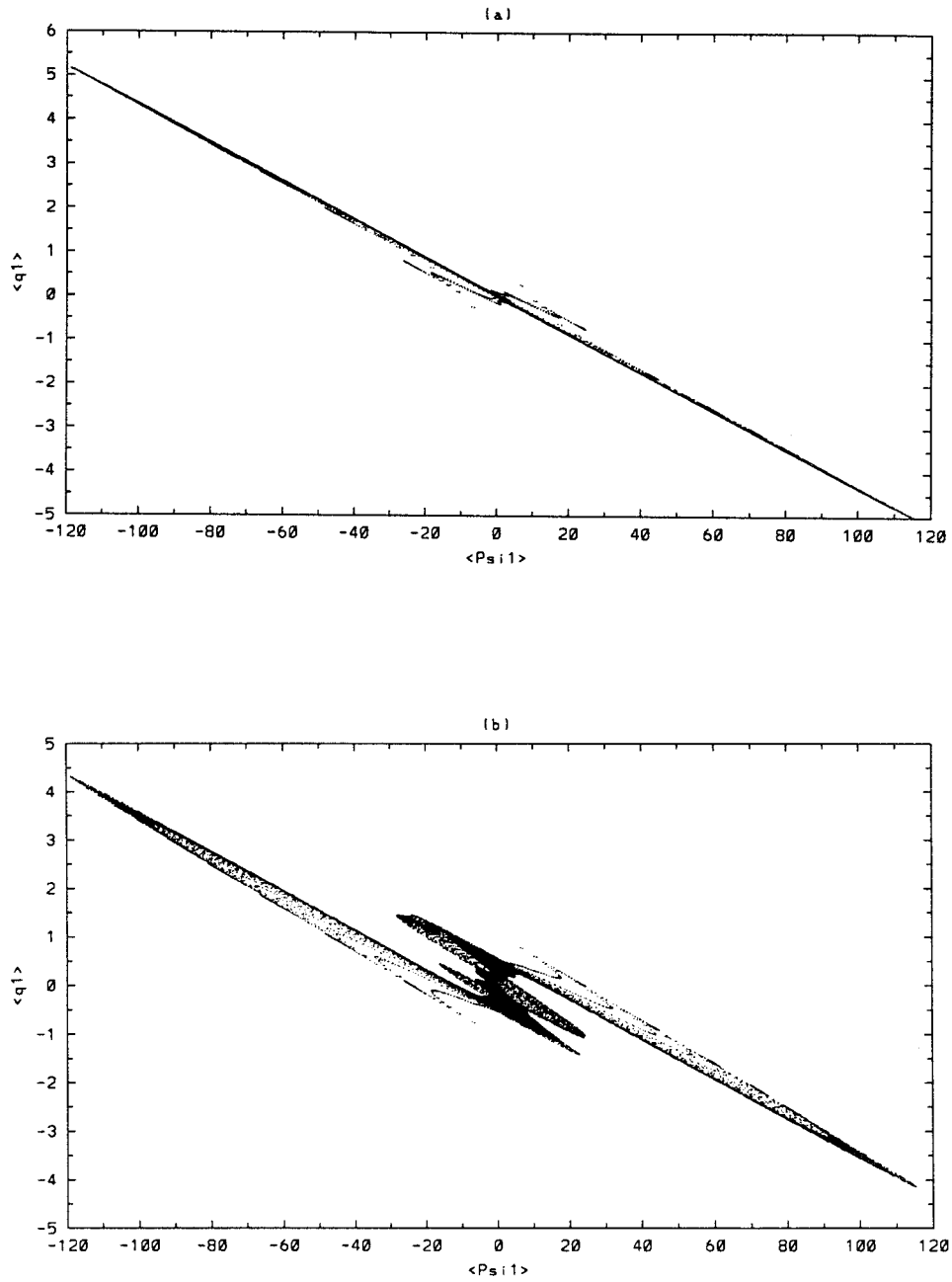$$\left. + \frac{F}{\delta(1 - \delta)}y + d_1y\right), \qquad (14)$$

FIG. 14. Contributions of the stretching and beta terms to the $\overline{\psi_1}-\overline{q_1}$ scatter diagram in the upper layer for expt V: (a) $\overline{q_1} = -\delta^{-1}F\overline{\psi_1}$ and (b) $\overline{q_1} = y - \delta^{-1}F\overline{\psi_1}$. In both cases, the slope is approximately equal to $-10/240$.

$$\psi_2^i(y) = \frac{1}{\det}\left(-\frac{F}{1-\delta}c_2 - c_2 d_2 - \frac{F}{\delta}d_2 \right.$$

$$\left. + \frac{F}{\delta(1-\delta)}y + c_1 y\right), \qquad (15)$$

where

$$\det = F\left(\frac{d_1}{\delta} + \frac{c_1}{1-\delta}\right) + c_1 d_1. \qquad (16)$$

The corresponding interior zonal velocities are

$$U_1^i = -\frac{d\psi_1^i}{dy} = -\frac{1}{\det}\left[\frac{F}{\delta(1-\delta)} + d_1\right], \qquad (17)$$

(a) <Psi1>

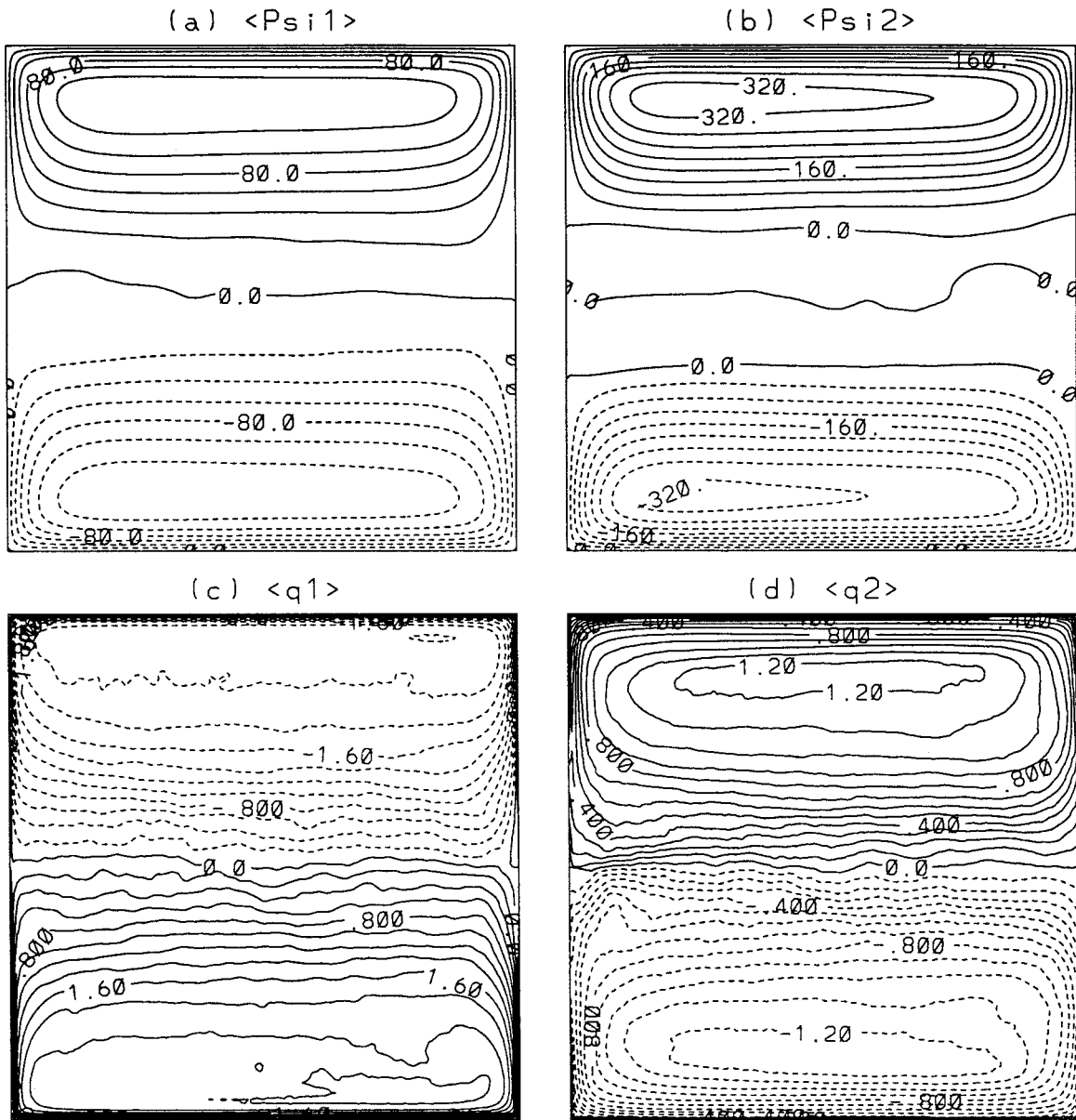
(b) <Psi2>

(c) <q1>

(d) <q2>

FIG. 15. (a) Upper-layer mean transport streamfunction (CI = 20 Sv), (b) lower-layer mean transport streamfunction (CI = 40 Sv), (c) upper-layer mean potential vorticity (nondimensional; CI corresponds to 0.6×10^{-6} s^{-1}), and (d) lower-layer mean potential vorticity (nondimensional; CI corresponds to 2.6×10^{-6} s^{-1}) for expt VI.

$$U_2^i = -\frac{d\psi_2^i}{dy} = -\frac{1}{\det}\left[\frac{F}{\delta(1-\delta)} + c_1\right]. \quad (18)$$

In order for the interior flow to be westward, in agreement with Fofonoff flows, the following conditions must be satisfied:

$$U_1^i < 0: \quad d_1 > -\frac{F}{\delta(1-\delta)} \quad \text{and} \quad \det > 0$$

or

$$d_1 < -\frac{F}{\delta(1-\delta)} \quad \text{and} \quad \det < 0, \quad (19)$$

$$U_2^i < 0: \quad c_1 > -\frac{F}{\delta(1-\delta)} \quad \text{and} \quad \det > 0$$

or

$$c_1 < -\frac{F}{\delta(1-\delta)} \quad \text{and} \quad \det < 0. \quad (20)$$

For Fofonoff flows to exist in both layers, U_1^i and U_2^i must be negative simultaneously. This condition can be
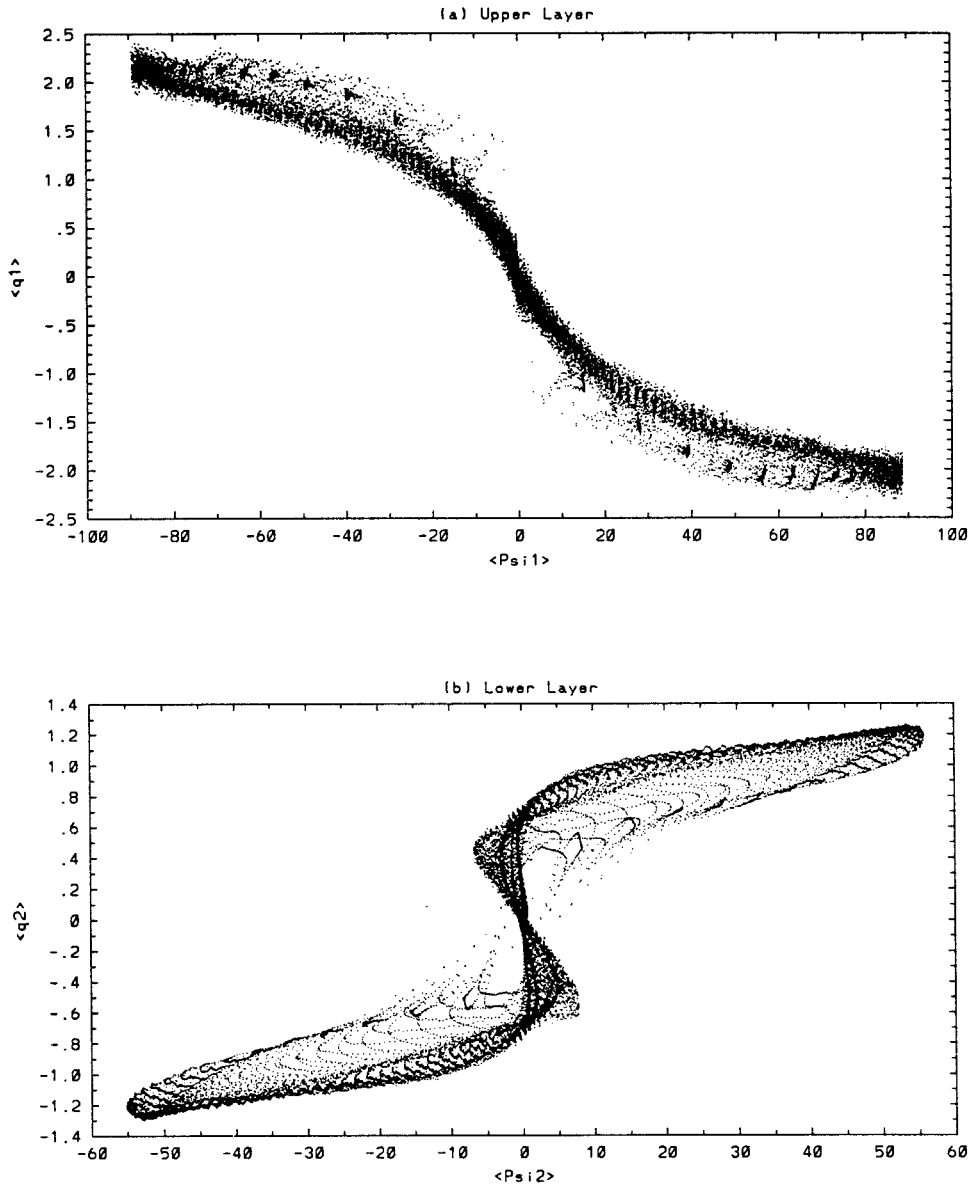
FIG. 16. Scatterplot of mean streamfunction versus potential vorticity (nondimensional) for expt VI (a) in the upper layer and (b) in the lower layer.

visualized by plotting the zonal interior velocities U_1^i and U_2^i as functions of c_1 and d_1 in Figs. 19a,b, respectively. Comparison of Figs. 19a and 19b indicates that the zonal velocities are both negative only in the upper-right quadrant. This region is defined by the hyperbola

$$c_1 > -\frac{F}{\delta}\frac{d_1}{[d_1 + F/(1-\delta)]}, \qquad (21)$$

as displayed in Fig. 19c. The shaded area shows the region in which Fofonoff flows are allowed in a two-layer quasigeostrophic model. This figure also demonstrates that unlike the barotropic case, the slopes do not necessarily need to be positive, but that zero (i.e., ho-mogenized potential vorticity) as well as negative slopes are allowed. The latter is a consequence of the stratification ($F > 0$).

The approximate slopes derived from experiments IV and VI show that they are within the shaded area, and that the flow patterns in these experiments are therefore consistent with Fofonoff flows (Fig. 19c).

For the flow regime generated in experiments V and VII, the lower-layer flow is very weak, and the upper-layer potential vorticity equation can be written as

$$q_1 = R\nabla^2\psi_1 + y - \frac{F}{\delta}\psi_1 = c_1\psi_1 + c_2. \qquad (22)$$

Again neglecting the relative vorticity, the interior
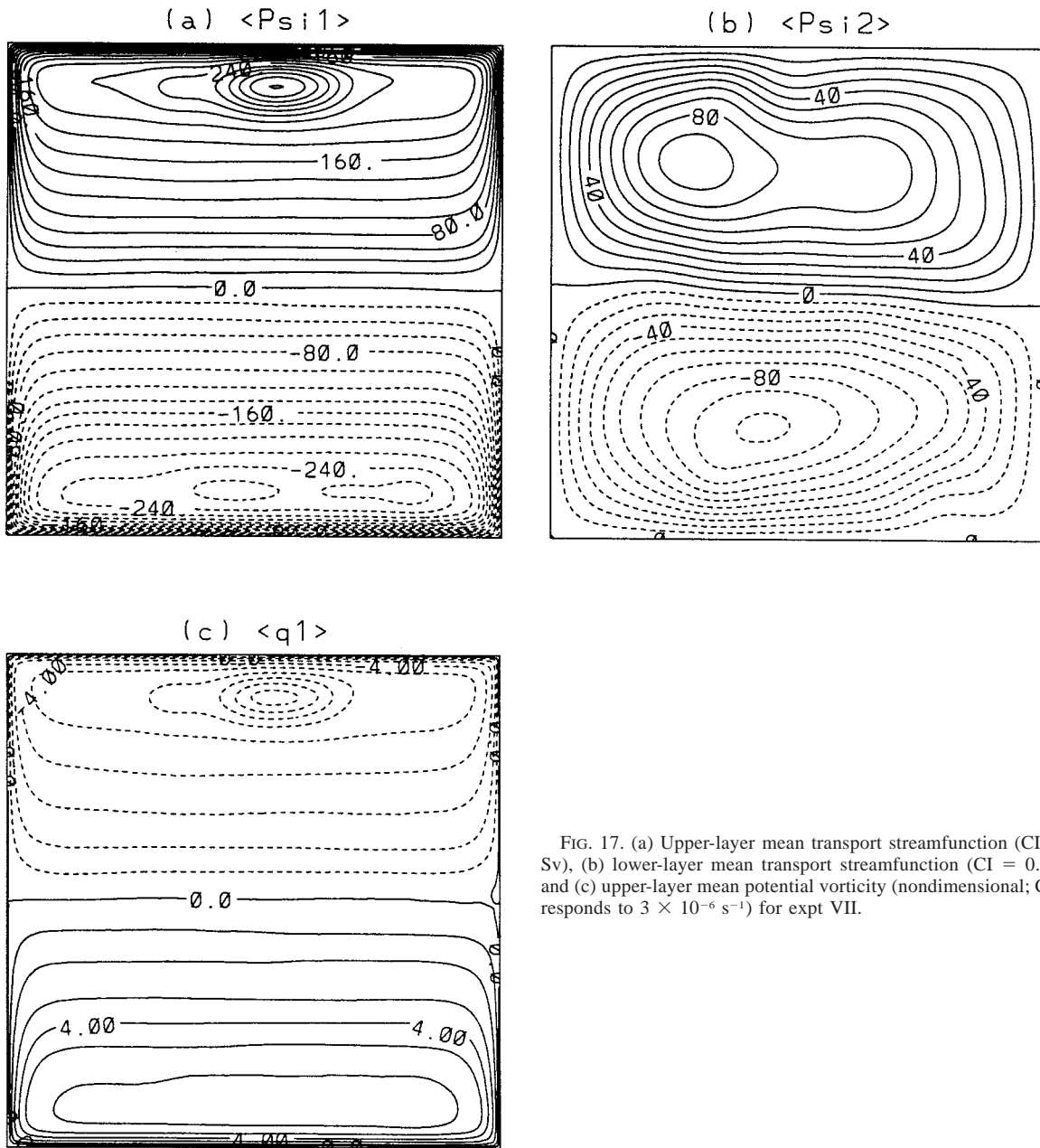
(a) <Psi1>

(b) <Psi2>

(c) <q1>

FIG. 17. (a) Upper-layer mean transport streamfunction (CI = 20 Sv), (b) lower-layer mean transport streamfunction (CI = 0.1 Sv), and (c) upper-layer mean potential vorticity (nondimensional; CI corresponds to 3×10^{-6} s^{-1}) for expt VII.

streamfunction can be expressed as $\psi_1^i(y) = (y - c_2)/(c_1 + F/\delta)$. The interior velocity $U_1^i = -1/(c_1 + F/\delta)$ will be westward as long as $c_1 > -F/\delta$. Note that this flow regime is a special case of the more general equation [Eq. (21)] when $d_1 \to \infty$ as $\psi_2 \to 0$. In experiments V and VII, the slope is slightly larger than $-F/\delta = -4.2 \times 10^{-2}$, and the flow patterns in experiments V and VII are therefore consistent with Fofonoff flows.

For $c_2 = 0$, the symmetric Fofonoff solution is recovered (Fig. 1a). Other values for c_2 result in asymmetric flow patterns, usually associated with nonzero total vorticity in the initial conditions or forcing (GS).

It is worth noting that Marshall and Nurser (1986) assumed $c_2 = 1$ (or βl in dimensional units) for the northern half and $c_2 = -1$ for the southern half of the domain, for which case the flow pattern is illustrated in Fig. 1b. In this case, the boundary layers are in the middle of the domain in the form of a midlatitude jet. This solution was found to be unstable in our experiments (section 4).

6. Summary and conclusions

In this paper, the emergence of Fofonoff-like flows over a wide range of dissipative parameter regimes has
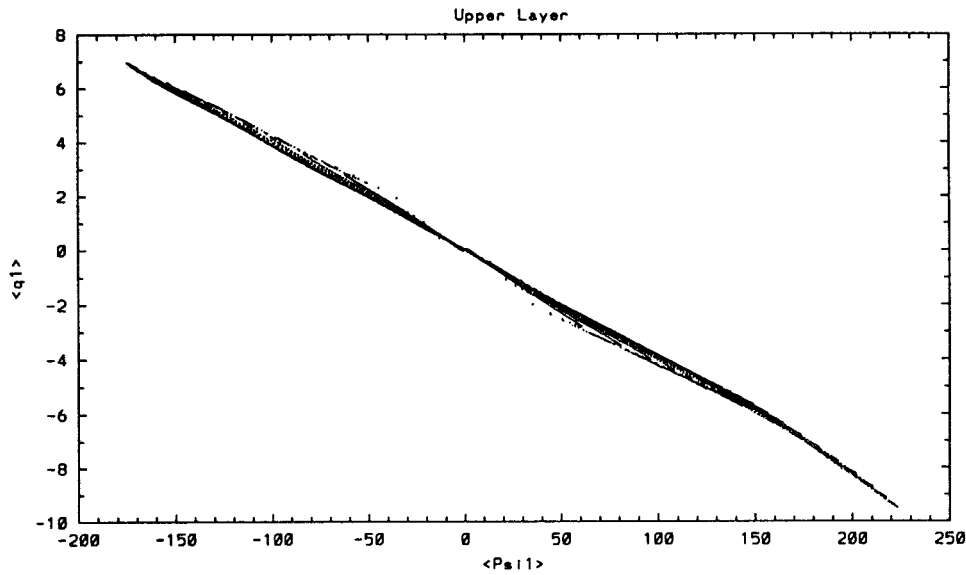
Fig. 18. Scatterplot of mean streamfunction versus potential vorticity (nondimensional) in the upper layer for expt VII.

been explored in a wind-driven two-layer quasigeostrophic model. Most of the previous work on this topic was performed either in the absence of forcing and dissipation or with a barotropic model. In a series of experiments performed with this two-layer model, two regimes were found in which Fofonoff-like circulations emerged. This is a direct consequence of the baroclinic nature of the system, as the wind forcing used in these experiments has been shown to inhibit the formation of Fofonoff flows in the barotropic case.

The "original" Fofonoff flows are defined for a barotropic ocean (Fofonoff 1954) and are characterized by a linear relationship between the streamfunction and vorticity, $q = c_1\psi + c_2$ with $c_1 > 0$. The flow pattern of these gyres is exhibited in Fig. 1a. Marshall and Nurser (1986) defined "generalized" Fofonoff flows in a baroclinic ocean such that $q_1 = c_1\psi_1 + c_2$ with $c_1 < 0$ in the upper layer, and the lower-layer potential vorticity is homogenized. These solutions are characterized by midlatitude gyres with a sense of direction opposite to the original Fofonoff flows (Fig. 1b). In this study, the range of the proportionality constants for the existence of Fofonoff-like flows in a two-layer quasigeostrophic model is derived. Provided that the gyres are consistent with the sense of direction and location of the original Fofonoff flows, it is shown that the proportionality constant between the streamfunction and potential vorticity can be positive, negative, or zero in both layers. We refer to "Fofonoff-like" gyres in a two-layer ocean as those satisfying the derived criteria.

The first regime in which Fofonoff-like gyres emerge is one in which the magnitudes of the frictional coefficients (viscosity and bottom dissipation) are extremely small. In this case, Fofonoff-like flows emerge despite

the fact that the wind forcing acts in a direction that was shown to prevent the emergence of Fofonoff flows in the barotropic context (GS). In the two-layer model, the wind forcing acts on the upper layer and does not force the lower layer directly. Fofonoff-like flows first appear in the lower layer and then spread throughout the water column via barotropization. The series of experiments presented in section 4 clearly illustrates the transition of the numerical solution from a conventional wind-driven circulation to an inertial Fofonoff-like regime. In these experiments, the mean signatures of the midlatitude jet and the associated recirculating gyres disintegrate as the magnitudes of the frictional parameters are reduced. The solution proposed by Marshall and Nurser (1986) was found to be unstable in this parameter regime.

Surprisingly, Fofonoff-like flows are also obtained with very high bottom friction. Inertial gyres appear only in the upper layer, as the lower layer is quasimotionless and acts as a sink of energy. This case is inherently different from a reduced-gravity model, in which the bottom layer is motionless and hence cannot dissipate energy. This result indicates that entropy can be maximized independently in each layer, depending on the distribution of forcing and dissipation. This brings a new perspective to the common assumption that forcing and dissipation are disruptive effects that prevent the system from displaying a Fofonoff-like state. The nature of these gyres in both cases is confirmed by reversing the wind forcing such that it favors Fofonoff flows. In both cases, the inertial gyres became more dominant, as expected for Fofonoff flows according to GS.

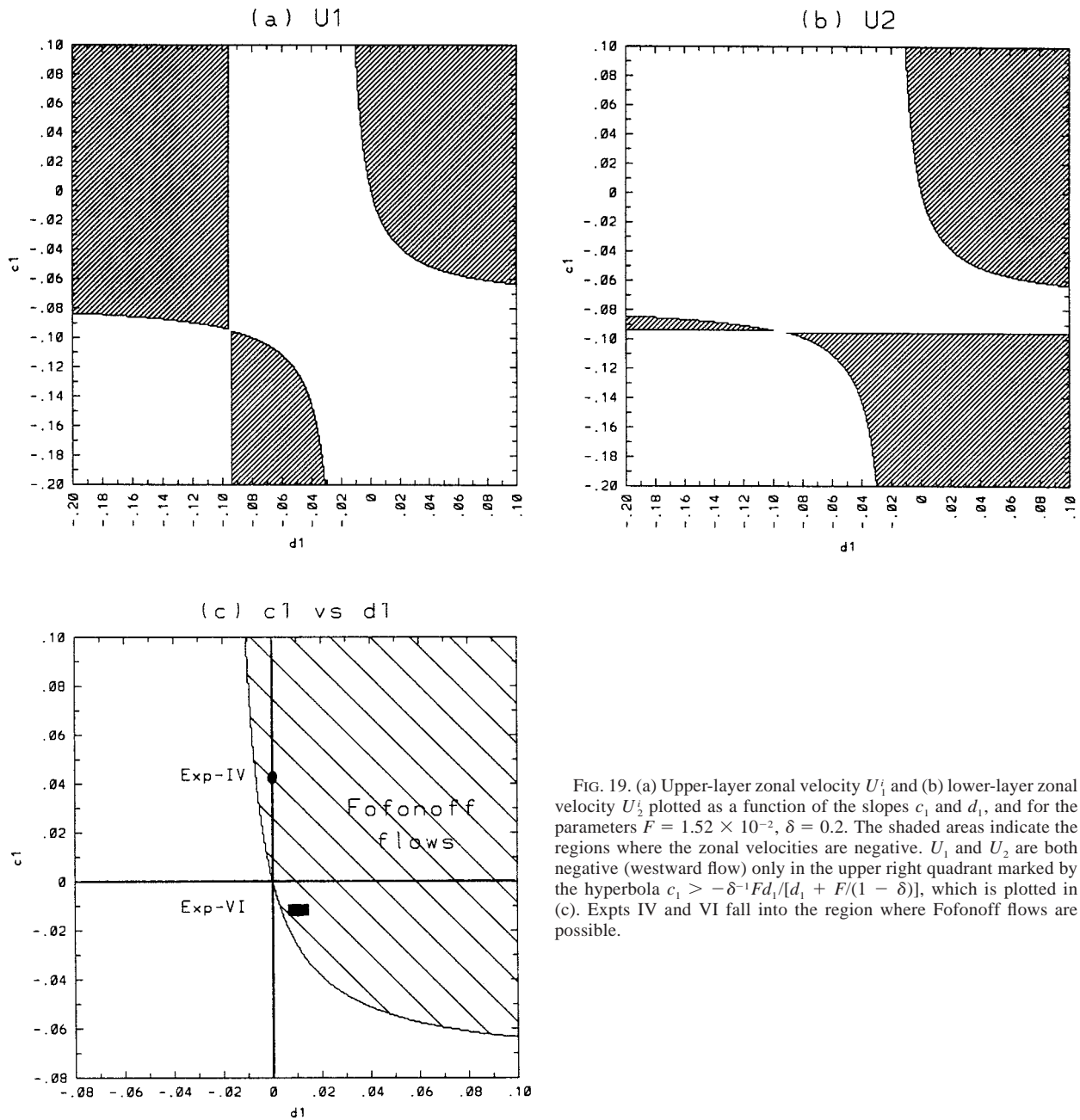In conclusion, the experiments presented in this paper

(a) U1

(b) U2

(c) c1 vs d1

FIG. 19. (a) Upper-layer zonal velocity U_1^i and (b) lower-layer zonal velocity U_2^i plotted as a function of the slopes c_1 and d_1, and for the parameters $F = 1.52 \times 10^{-2}$, $\delta = 0.2$. The shaded areas indicate the regions where the zonal velocities are negative. U_1 and U_2 are both negative (westward flow) only in the upper right quadrant marked by the hyperbola $c_1 > -\delta^{-1}Fd_1/[d_1 + F/(1 - \delta)]$, which is plotted in (c). Expts IV and VI fall into the region where Fofonoff flows are possible.

suggest that Fofonoff-like solutions appear over a much wider spectrum of forcing and dissipation than was initially implied by the theory based on equilibrium statistical mechanics (SHH) and by previous studies that solely relied on barotropic models. The present results are obtained in a parameter range that is not realistic, but they indicate the presence of a fundamental mechanism that might have an impact on the ocean general circulation. Therefore, a logical next step would be a systematic investigation of the appearance of these so-

lutions in a realistic configuration under generalized forcing and dissipation, with special emphasis on their impact upon the ocean general circulation.

REFERENCES

Arakawa, A., 1966: Computational design for long-term numerical integration of the equations of fluid motion: Two dimensional incompressible flow. Part I. *J. Comput. Phys.,* **1,** 119–143.

Barnier, B., B. L. Hua, and C. Le Provost, 1991: On the catalytic role of high baroclinic modes in eddy-driven large-scale circulations. *J. Phys. Oceanogr.,* **21,** 976–997.

Böning, C. W., 1986: On the influence of frictional parameterization in wind-driven circulation models. *Dyn. Atmos. Oceans,* **10,** 63–92.

Bretherton, F. P., and D. B. Haidvogel, 1976: Two dimensional turbulence above topography. *J. Fluid Mech.,* **78,** 129–154.

Carnevale, G. F., and J. D. Fredericksen, 1987: Nonlinear stability and statistical mechanics of flow over topography. *J. Fluid Mech.,* **175,** 157–181.

Cessi, P., 1991: Laminar separation of colliding western boundary currents. *J. Mar. Res.,* **49,** 697–717.

——, R. V. Condie, and W. R. Young, 1990: Dissipative dynamics of western boundary layers. *J. Mar. Res.,* **48,** 677–700.

Chassignet, E. P., 1995: Vorticity dissipation by western boundary currents in the presence of outcropping layers. *J. Phys. Oceanogr.,* **25,** 242–255.

——, and R. Bleck, 1993: The influence of layer outcropping on the separation of boundary currents. Part I: The wind-driven experiments. *J. Phys. Oceanogr.,* **23,** 1485–1507.

Cummins, P. F., 1992: Inertial gyres in decaying and forced geostrophic turbulence. *J. Mar. Res.,* **50,** 545–566.

Fofonoff, N. P., 1954: Steady flow in a frictionless homogeneous ocean. *J. Mar. Res.,* **13,** 254–262.

Gazdag, J., 1976: Time-differencing schemes and transform methods. *J. Comput. Phys.,* **20,** 196–207.

Griffa, A., and R. Salmon, 1989: Wind-driven ocean circulation and equilibrium mechanics. *J. Mar. Res.,* **47,** 457–492.

——, E. P. Chassignet, V. Coles, and D. B. Olson, 1996: Inertial gyre solutions from a primitive equation ocean model. *J. Mar. Res.,* **54,** 653–677.

Harrison, D. E., and W. R. Holland, 1981: Regional eddy vorticity transport and the equilibrium vorticity budgets of a numerical model ocean circulation. *J. Phys. Oceanogr.,* **11,** 190–208.

Holland, W. R., 1978: The role of mesoscale eddies in the general circulation of the ocean. *J. Phys. Oceanogr.,* **8,** 363–392.

——, and W. J. Schmitz, 1985: Zonal penetration scale of model midlatitude jets. *J. Phys. Oceanogr.,* **15,** 1859–1875.

Marshall, J., and G. Nurser, 1986: Steady, free circulation in a stratified quasi-geostrophic ocean. *J. Phys. Oceanogr.,* **16,** 1799–1813.

Pedlosky, J., 1987: *Geophysical Fluid Dynamics.* 2d ed. Springer-Verlag, 624 pp.

Rhines, P. B., and W. Young, 1982: A theory of wind-driven circulation I—Mid-ocean gyres. *J. Mar. Res.,* **40,** 559–596.

Richardson, P. L., 1983: Eddy kinetic energy in the North Atlantic from surface drifters. *J. Geophys. Res.,* **88**(C7), 4355–4367.

Richardson, W. S., W. J. Schmitz Jr., and P. P. Niiler, 1969: The velocity structure of the Florida Current from the Straits of Florida to Cape Fear. *Deep-Sea Res.,* **16**(Suppl.), 225–231.

Salmon, R., G. Holloway, and M. C. Hendershott, 1976: The equilibrium statistical mechanics of simple quasi-geostrophic models. *J. Fluid Mech.,* **75,** 691–703.

Thompson, J. D., and W. J. Schmitz Jr., 1989: A limited-area model of the Gulf Stream: Design, initial experiments, and model-data intercomparison. *J. Phys. Oceanogr.,* **19,** 791–814.

Veronis, G., 1966: Wind driven ocean circulation. Part 2. Numerical solution of a nonlinear problem. *Deep-Sea Res.,* **13,** 31–55.

Verron, J., and C. Le Provost, 1991: Response of eddy-revolved general circulation numerical models to asymmetrical wind forcing. *Dyn. Atmos. Oceans,* **15,** 505–533.

Wang, J., and G. K. Vallis, 1994: Emergence of Fofonoff states in inviscid and viscous ocean circulation models. *J. Mar. Res.,* **52,** 83–127.